# Gas−Liquid Interfacial Mass Transfer in Trickle-Bed Reactors at Elevated Pressures

**F. Larachi***,†

*Department of Chemical Engineering & CERPIC, Laval University, Sainte-Foy, Québec, Canada G1K 7P4*

**M. Cassanello**‡

*PINMATE, Departamento de Industrias, FCEyN, Universidad de Buenos Aires, 1428 Ciudad Universitaria, Buenos Aires, Argentina*

**A. Laurent**§

*Laboratoire des Sciences du Génie Chimique, CNRS, ENSIC, INPL, 1 Rue Grandville, BP 451, 54001 Nancy Cédex, France*

A phenomenological description and a semiempirical two-zone model are proposed for the gas−liquid interfacial areas and the volumetric liquid-side mass-transfer coefficients in cocurrent downflow trickle-bed reactors operated at elevated pressure. Gas−liquid interfacial areas, $a$, and volumetric liquid-side mass-transfer coefficients, $k_La$, are measured in the trickle flow regime at high nitrogen pressure (0.3−3.2 MPa). Use is made of diethanolamine carbamation in aqueous viscous and organic model solutions in which fast and slow absorptions of carbon dioxide occur. In order to extract genuine mass-transfer parameters, a rigorous thermodynamic model is established to account for liquid and gas nonidealities. The influence of pressure, gas and liquid superficial velocities, liquid viscosity, and packing size on the gas−liquid interfacial mass transfer is examined. At constant gas and liquid superficial velocities, increasing the reactor pressure improves the gas−liquid interfacial mass transfer at the expense of increased two-phase pressure drop and gas holdup. At high pressure, the gas−liquid flow may be viewed as a two-zone flow pattern: (i) a liquid-free gas continuous phase which delineates a macroscopic gas−liquid interface (ii) and a gas−liquid film emulsion comprised of tiny bubbles which form in the films and delineate a microscopic gas−liquid interface. Taylor's theory of fluid−fluid sheared emulsions is used to quantify the microscopic interface via the effect of pressure on the size of bubbles in the trickling film. A bubble Sauter diameter is related to viscous shear stress and surface tension force, the two competing forces that determine bubble size. The model is also extended to estimate volumetric gas−liquid mass-transfer coefficients under high-pressure conditions.

## Introduction

Trickle-bed reactors (TBRs) are among the most widely encountered three-phase contactors in industrial practice. They are mainly employed in the petroleum and petrochemical industries, wastestream treatment, chemical industries, biochemical and electrochemical processing, etc. Some of the specific commercial applications of TBRs include processing of various oil fractions such as in hydrorefining and catalytic hydrofinishing, oxidation of organics in wastewater effluents, VOC abatement in air pollution control, and enzymatic reactions. The majority of commercial TBRs operate at elevated pressure and temperature, i.e., conditions where there is still a need for experimental information on their key parameters.

A TBR consists of a vertical column containing a fixed bed of randomly packed catalyst pellets contacted by a cocurrent gas−liquid downflow carrying both the reactants and products. When the gas and liquid are fed cocurrently upward through the packed bed, the system is termed a flooded bed reactor (FBR). Owing to a motionless catalyst bed, near plug flow is achieved in TBRs, and in that respect they are superior to other three-phase reactors where the catalyst is either slurried or fluidized. Moreover, TBRs' high catalyst loading per unit volume of the liquid and low-energy dissipation rate make them preferable to slurry reactors. Probably the only marked disadvantages of TBRs are their impracticality for reactions with rapidly deactivating catalysts and the possibility of liquid maldistribution.

In three-phase gas−liquid−solid systems such as in a TBR, the gas−liquid mass-transfer resistance can have a detrimental effect on the global reaction rate. Accurate evaluation of the gas−liquid mass-transfer parameters is, therefore, essential for achieving a successful reactor design and scaling. Earlier investigations of gas−liquid mass-transfer characteristics of TBRs were mostly limited to atmospheric pressure (Gianetto et al., 1973; Hirose et al., 1974; Charpentier, 1976; Fukushima and Kusaka, 1977; Bakos et al., 1980; Morsi et al., 1980, 1984; Midoux et al., 1984; Morsi, 1989; Venkata Ratnam and Varma, 1991; Wild et al., 1992; Venkata Ratnam et al., 1994). Only a few researchers

---

* Author to whom correspondence is addressed.

[†] E-mail: flarachi@gch.ulaval.ca. Phone: 418-656-3566. Fax: 418-656-5993.

[‡] E-mail: miryan@di.fcen.uba.ar. Phone/Fax: (+54-1) 784 0208.

[§] E-mail: alaurent@ensic.u-nancy.fr. Phone: 33-3-83-17-52-06. Fax: 33-3-83-32-29-75.

S0888-5885(96)00903-7 CCC: $15.00

have studied how gas–liquid mass transfer evolves at elevated pressures (Wammes and Westerterp, 1991; Wammes et al., 1991; Wild et al., 1992; Larachi et al., 1992; Lara-Marquez et al., 1992; Cassanello et al., 1996). From these studies, it was established that gas–liquid interfacial areas and volumetric liquid-side mass-transfer coefficients may be greatly affected by the pressure level in the reactor.

In general, attempts to interpret the influence of pressure on the hydrodynamics of TBRs remain embryonic and qualitative. Two viewpoints have been put forward. For the first one, changes on parameters such as liquid holdup, wetting efficiency, or gas–liquid interfacial area with pressure have been interpreted using bed-scale force arguments (Al-Dahhan and Duduković, 1994, 1995; Wammes and Westerterp, 1991; Wammes et al., 1991). Resisting frictional forces at the packing surface and driving forces, namely, pressure gradient and liquid gravitational force, affects energy dissipation in the reactor and consequently all the TBR hydrodynamic parameters. The second viewpoint ascribes the changes in TBR parameters to pore-scale phenomena (Larachi et al., 1992). It has been observed experimentally that, below a critical value of superficial gas velocity, gas holdup and mass-transfer parameters are unaffected by pressure. Beyond this critical velocity, increasing pressure enhances these parameters. This observation has been qualitatively interpreted assuming that, besides improving liquid spreading over the packing, high pressures also bring about high gas–liquid interfacial shears. As a result of the high momentum transfer, some gas is entrained and dispersed under the form of tiny bubbles in the liquid, thereby enhancing gas–liquid mass transfer and gas holdup.

In recent studies, the main interest in TBR modeling concerned flow regime transitions (Ng, 1986; Dankworth et al., 1990), liquid holdup, and two-phase pressure drop (Crine et al., 1992; Holub et al., 1993). A mass-transfer model has recently been developed by Toppinen et al. (1996) using the Maxwell–Stefan equations and the film theory to simulate a large-scale TBR for the hydrogenation of toluene in multicomponent liquid and gas phases. From analysis of the literature it can be concluded that almost no theoretical studies have been attempted to interpret and to quantify the effect of pressure on gas–liquid mass transfer in TBRs. In addition, available experimental data have often been restricted to atmospheric conditions. It is, therefore, recommended to obtain high-pressure mass-transfer data using different liquid properties and packing characteristics in order to develop a trustful mass-transfer modeling.

In this work, gas–liquid interfacial areas and volumetric liquid-side mass-transfer coefficients are measured in a trickle-bed reactor operated between 0.3 and 3.2 MPa in the trickle flow regime and at the transition between trickling and pulsing. Effects of liquid viscosity and particle size and shape on gas–liquid interfacial areas are studied.

A simple two-zone semiempirical model is proposed to explain the increase of gas–liquid mass transfer driven by pressure effects. It is based on the pore-scale force arguments discussed above. An expression to estimate a mean bubble diameter is derived based on the theory of fluid emulsions. The model is also extended to estimate $k_La$ in TBRs at high pressure.

**Survey of Gas–Liquid Mass Transfer in Pressurized Contactors.** Contrary to TBRs, available information on gas–liquid mass transfer at elevated pressure is more extensive for other gas–liquid and gas–liquid–solid contactors such as for bubble columns (BC), autoclaves (AC), agitated reactors (AR), packed bubble columns (PBC), and agitated slurry reactors (ASR). A survey of existing studies of pressure effects on gas–liquid mass-transfer characteristics ($a$ and $k_La$) in such different gas–liquid and gas–liquid–solid systems is given in Table 1. The main conclusions arising from these studies are pinpointed hereafter.

(a) As a general rule, an increase in pressure induces an increase in $a$ and $k_La$.

(b) In BCs and in TBRs, the influence of pressure on the gas–liquid mass-transfer parameters is negligible for very low gas superficial velocities.

(c) In BCs, it is established that an increase in pressure reduces significantly bubble size, which thus results in an increase of both interfacial areas and gas holdups at constant superficial gas velocity.

(d) The majority of studies have concluded that the liquid-side mass-transfer coefficient, $k_L$, is insensitive to pressure up to 4 MPa. Atypical trends have, however, been pinpointed for the $k_La$–pressure relationship for some particular organic liquids and temperatures in flat-interface vessels where, in principle, $a$ is only geometry-dependent (Chang et al., 1991; Chang and Morsi, 1991a,b, 1992; Mizan et al., 1994; Koneripalli et al., 1994). The different trends of $k_La$ dependencies were attributed to possible variation of $k_L$ with pressure-dependent liquid diffusion coefficient, liquid viscosity, and surface tension (Tekie et al., 1997). Nevertheless, as the mass-transfer coefficient $k_L$ was not measured directly and independently, there is no clear evidence in favor of a $k_L$ depending on pressure.

## Experimental Section

**Setup.** A simplified flow diagram of the experimental setup is shown in Figure 1. The reactor is operated with the gas and liquid flowing cocurrently downward. The maximum operating pressure withstood by the setup is 5 MPa. Mass-transfer experiments are performed in a cylindrical reactor of 400 mm height and 23 mm internal diameter. The reactor consists of two 200-mm-high stainless steel modules fitted with flanges. Several porous and nonporous packings differing in size, shape, and roughness have been used (see Table 2a). To ensure a good radial distribution of the liquid at the entrance, the reactor is topped with a 100-mm-high prepacking section containing 3 mm glass beads (see Figure 1). At the bottom of the prepacking section gas is injected from two 180°-spaced holes located in the upper flange. Just below the bed supporting grid, the gas phase can be analyzed using a specially designed sampling device which prevents liquid to be entrained once a gas sample is withdrawn. The sampling device consists of a baffled cell and a chromatography-like loop composed of two three-way pneumatic valves controlled by a timer that switches the flow from one segment to the other segment of the loop. Gas flows continuously through the sampling device, and a draining is opened regularly to evacuate the accumulated liquid. Only when no liquid is drained is the gas phase analyzed.

**Liquid Solutions and Liquid Circuit.** Interfacial areas are determined using chemical absorption of $CO_2$ into 1.5 kmol/m$^3$ diethanolamine (DEA) aqueous solutions. The viscosity of the liquid is changed by adding 20% and 40% of ethylene glycol (ETG; mass percentage

**Table 1. Studies of the Gas−Liquid Mass-Transfer Characteristics in Various High-Pressure Gas−Liquid and Gas−Liquid−Solid Contactors**

| GL/GLS contactor | ref | pressure range and gas−liquid system | pressure effect on parameters[a] | | | remarks |
|---|---|---|---|---|---|---|
| | | | $a$ | $k_La$ | $k_L$ | |
| BC−AR | Vafopoulos (1975) | | | − | | only low gas velocities |
| BC | Wilkinson et al. (1994) | $P = 0.1-1.5$ MPa; gases: He, $N_2$, Ar, $CO_2$, $SF_6$; liquids; ETG, water, *n*-heptane | ↑ | ↑ | ns | Sauter diameter decrease with gas density and increase with liquid viscosity |
| AR | Teramoto et al. (1974) | $P = 0.2-10$ MPa; gases; $N_2$, $O_2$; liquid; water | | − | | |
| AR | Albal et al. (1984) | $P = 1.0-3.5$ MPa; gases; $H_2O$, CO; liquid; molten wax | | − | | |
| AR | Ledakowicz et al. (1984) | $P = 0.5-6$ MPa; gases; $H_2$, $N_2$, CO, $CO_2$; liquid; molten wax | ns | − | ns | |
| AR | Lee and Foster (1990a,b) | $P = 1.0-7.0$ MPa; gases; $O_2$, $CH_4$; liquid; silicone fluid | | ↑ | | |
| AR | Chang et al. (1991) | $P = 0.1-5.0$ MPa; gases; $N_2$, $CH_4$, $H_2$; liquid; *n*-hexane | ns | (*) | ns | (*) the effect of $P$ on $k_La$ depends on the system |
| AR | Chang and Morsi (1991a) | $P = 0.1-5.5$ MPa; gases; $H_2$, $N_2$, $CH_4$; liquid; *n*-decane | ns | (*) | ns | |
| AR | Stegeman et al. (1995) | $P = 0.3-6.6$ MPa; gas; $CO_2/N_2$; liquid; DEA in water and water/ETG | − | ns | ns | experiments in the regime of high agitation rates; $a$ decreases with liquid viscosity |
| AC | Bichari et al. (1991, 1993, 1996) | $P = 0.1-5.0$ MPa; gas; $CO_2/N_2$; liquid; water/sucrose, water/CMC, water/NaCl, water/$Na_2SO_4$ | ns | − | − | |
| ASR | Miller et al. (1990) | $P = 1-3$ MPa; gas; $H_2$, CO; liquid; *n*-$C_{28}H_{58}$ | ns | − | ns | |
| AC | Yoshida and Arakawa (1968) | $P = 0.1-2.0$ MPa; gas; $O_2$; liquid; water | ns | ↓ | ns | |
| AC | Chang and Morsi (1991b) | $P = 0.1-5.0$ MPa; gases; $N_2$, $CH_4$ liquid; *n*-hexane, water | ns | (*) | ns | |
| AC | Mizan et al. (1994) | $P = 1.1-5.5$ MPa; gases; $H_2$, ethylene; liquid; propylene | ns | (*) | ns | |
| AC | Koneripalli et al. (1994) | $P = 0.1-6.0$ MPa; gases; $H_2$, $N_2$, CO, $CH_4$, $CO_2$; liquids; methanol, ethanol | ns | (*) | ns | $k_La$ increases with pressure in most of the systems |
| ASR−AC | Albal et al. (1983) | $P = 0.5-9.7$ MPa; gases; $O_2$, He; liquid; water; solids; glass beads (75−500) $\mu$m), oil shale particles (44 $\mu$m) | | − | | |
| ASR−AC | Deimling et al. (1984) | $P = 1.0-4.0$ MPa; gases; $H_2$, CO; liquid: Fischer−Tropsch; solids: glass beads (125−177 $\mu$m) | ↑ | ↑ | − | effect of pressure on $k_La$ not changed by the addition of solids |
| ASR−AC | Karandikar et al. (1986) | $P = 1.0-4.0$ MPa; gases: $H_2$, CO, $CH_4$, $CO_2$; liquid: Fischer−Tropsch; solids: glass beads (125−177 $\mu$m) | ↑ | ↑ | − | effect of pressure on $k_La$ not changed by the addition of solids |
| ASR | Chang and Morsi (1992) | $P = 0.1-5$ MPa; $CH_4$/hexane; coal 28−200 mesh | ns | ↑ | ns | $k_La$ decreases with addition of solids and with increase in solids holdup |
| TBR | Wammes et al. (1991) | $P = 0.3-5.0$ MPa; gas: $CO_2/N_2$; liquids: DEA/water/antifoaming, DEA/40% ETG/water | ↑ | ns | ns | negligible influence of the liquid viscosity on $a$ |
| TBR | Larachi et al. (1992) | $P = 0.3-3.2$ MPa; gas: $CO_2/N_2$; liquids: DEA/0, 20,40% ETG/water, DEA/ETG | ↑ | ↑ | ns | |
| TBR | Lara-Marquez et al. (1992) | $P = 0.3-3.2$ MPa; gas: $CO_2/N_2$; liquids: DEA/0, 20, 40% ETG/water, DEA/ETG | ↑ | ↑ | ns | |
| PBC−AR | Oyevaar et al. (1991) | $P = 0.1-8.0$ MPa; gas: $CO_2/N_2$; liquid: water/DEA | ↑ | ns | ns | |
| FBR | Stüber et al. (1996) | $P = 0.1-0.4$ MPa; $H_2$/1,5,9-cyclododecatriene | ns | ↑ | ns | |
| BC | Stegeman et al. (1996) | $P = 0.1-6.6$ MPa; gas: $CO_2/N_2$; liquid: water/DEA | ↑ | ns | ns | |
| FBR | Molga and Westerterp (1997) | $P = 0.1-6.4$ MPa; gas: $CO_2/N_2$; liquid: DEA/water, DEA/40% ETG/water | − | ns | ns | |
| AR | Tekie et al. (1997) | $P = 0.1-4$ MPa; gas: $O_2$, $N_2$; liquid: cyclohexane | ns | ↑ | ns | |

[a] ↑: increases. ↓: decreases. −: independent. ns: not studied.

in the DEA-free water solutions). Volumetric liquid-side mass-transfer coefficients are measured using chemical absorption of $CO_2$ into a ETG solution of 0.05 kmol/m$^3$ DEA. All the experiments are carried out at pressures from 0.3 to 3.2 MPa, in the liquid mass flux range (1.4−8 kg/m$^2$·s) and the liquid superficial velocity range (0.14−0.77 cm/s). The DEA solutions are prepared with fresh diethanolamine (Merck, purity > 98%) mixed with ethylene glycol (Merck, purity > 99%) and deionized water (electrical conductivity < 20 $\mu$S/cm). The liquid solutions are pumped from a 40-L thermostated storage vessel into the TBR by means of a Milroyal−Dosapro reciprocating proportioning pump with an adjustable stroke length and a maximum flow rate of 194 L/min. The liquid is heated up and maintained at 298 K. To minimize pump pulsations, a guard packed column and a OLAER IHV 0.5 330 dumping device containing an EPDM membrane have been installed at

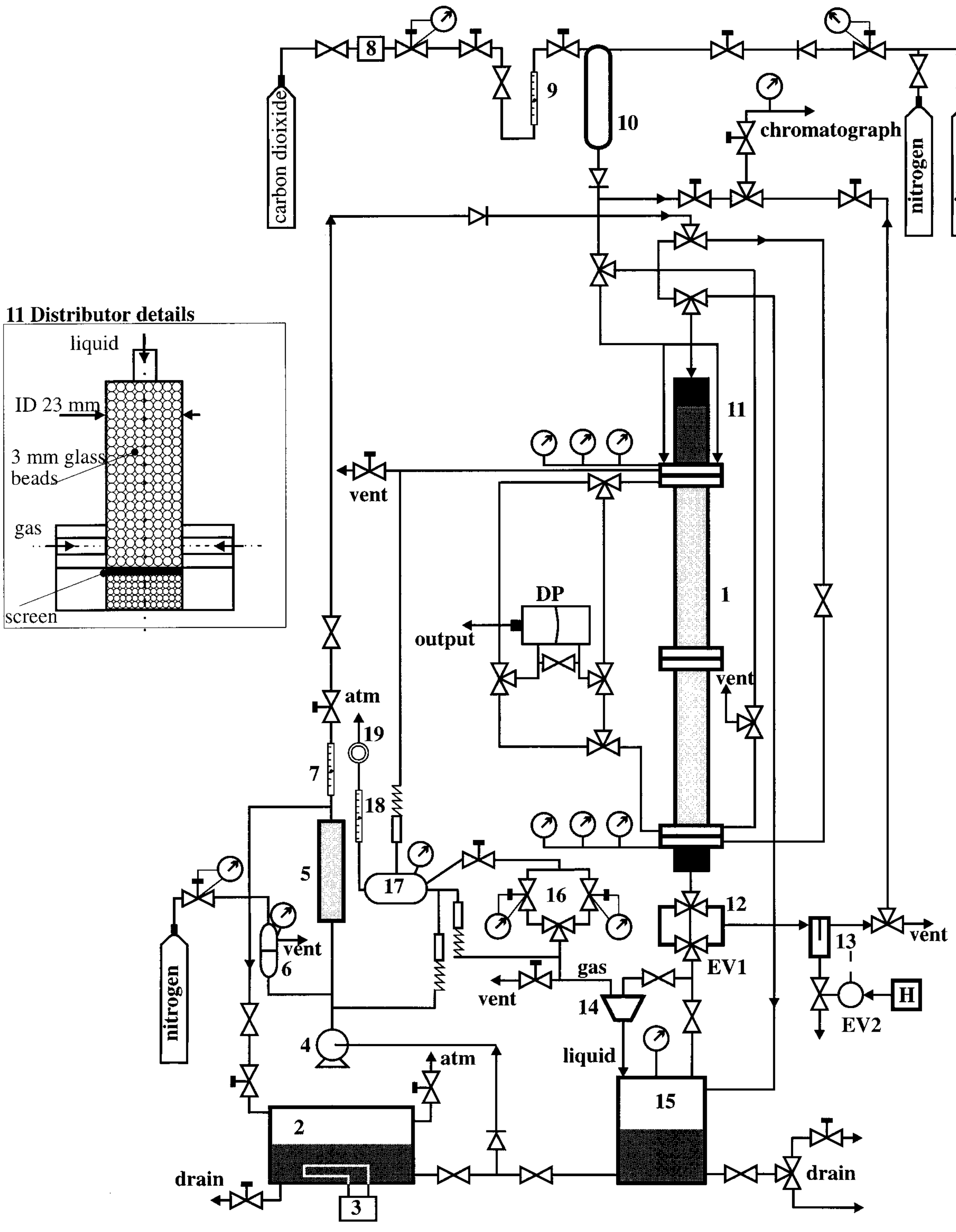

**1 Reactor - 2 Liquid atmospheric storage vessel - 3 Liquid heater - 4 Volumetric pump - 5 Damping device 1 - 6 Damping device 2 - 7 Liquid rotameter - 8 Gas heater - 9 CO2 high pressure rotameter - 10 Mixing chamber - 11 Distributor - 12 Gas sampler - 13 Liquid separator - 14 Cyclone separator - 15 High pressure storage and recycling vessel - 16 Upstream pressure controller - 17 Expansion vessel - 18 Gas rotameter - 19 Gas volumetric counter - DP differential pressure transmitter - EV electronic valve - H timer**

**Figure 1.** Schematic of the experimental high-pressure trickle-bed reactor facility.

the pump discharge. Liquid flow rate is measured by means of a Brooks HP 1410 R6 15A rotameter. After leaving the reactor, the liquid is separated from the gas in a cyclone, flows into a 40-L buffer vessel, and is then evacuated.

**Gas Mixture and Gas Circuit.** A mixture of 5% by volume $CO_2$ (Air Gaz, purity > 99.9%) in nitrogen (Air Gaz, purity>99.9%) is achieved by bringing the gases into contact in a mixing chamber. The $CO_2$ content in the feeding gas is regulated by means of the nitrogen pressure reducers and the $CO_2$ rotameter. The amount of $CO_2$ absorbed in the liquid phase is determined by measuring carbon dioxide inlet and outlet mole fractions in the gas stream by gas-phase chromatography (Haysep QS 80−100 mesh, 2-m long column). Gas upstream pressure controllers maintain the pres-

**Table 2.**

(a) Characteristics of the Packings Used in the Experiments

| packing | $d_e$ (mm) | bed porosity, $\epsilon$ (%) | sphericity[a] |
|---|---|---|---|
| porous activated carbon | 1.52 | 32 | 0.95 |
| alumina sphere | 2.0 | 39 | 1 |
| propylene extrudate[b] | 3.37 | 37 | 0.91 |
| glass beads | 0.85 | 35 | 1 |
| glass beads | 1.18 | 36 | 1 |
| glass beads | 1.98 | 37 | 1 |
| glass beads | 3.05 | 39 | 1 |

(b) Physicochemical Properties of the Liquid Solutions Employed

| liquid | $\rho_L$ (kg/m$^3$) | $\mu_L$ (mPa·s) | $\sigma_L$ (mN/m) | $P$ (MPa) | $10^9 D_A$[c] (m$^2$/s) | $10^9 D_B$[c] (m$^2$/s) |
|---|---|---|---|---|---|---|
| $CO_2$/DEA/$H_2O$ | 1016 | 1.2 | 64 | 0.3−3.1 | 1.7 | 0.76 |
| $CO_2$/DEA/$H_2O$ + 20% ETG | 1037 | 2.3 | 59 | 1.1 | 1.0 | 0.43 |
| $CO_2$/DEA/$H_2O$ + 40% ETG | 1061 | 3.8 | 57 | 0.3−2.1 | 0.7 | 0.26 |
| $CO_2$/DEA/ETG | 1112 | 18 | 48 | 0.3−3.2 | 0.3 | 0.15 |

[a] Sphericity = 4.836 ($V_p^{2/3}/A_p$). [b] Initially hydrophobic, hydrophilized by chemical cross-linking. [c] A = $CO_2$. B = DEA.

**Table 3. Liquid Thermodynamic Equilibria**[a]

$$K_b = \frac{\gamma_3\gamma_6}{\gamma_B a_w}\frac{m_3 m_6}{m_B} \tag{2}$$

$$K_{c1} = \frac{\gamma_5\gamma_1}{\gamma_A a_w}\frac{m_5 m_1}{m_A} \tag{3}$$

$$K_{c2} = \frac{\gamma_5\gamma_2}{\gamma_1}\frac{m_5 m_2}{m_1} \tag{4}$$

$$K_w = \frac{\gamma_5\gamma_6}{a_w} m_5 m_6 \tag{5}$$

$$K_h = \frac{\gamma_4 a_w}{\gamma_B\gamma_1}\frac{m_4}{m_B m_1} \tag{6}$$

$$\log(K_b) = \frac{-4019.2}{T} - 22.4773\log(T) - 0.004436T + 65.303 \tag{7}$$

$$\log(K_{c1}) = \frac{-5251.53}{T} - 36.7816\log(T) + 102.269 \quad (8)$$

$$\log(K_{c2}) = \frac{-5399.02}{T} - 35.4819\log(T) + 95.5739 \quad (8)$$

$$\log(K_w) = \frac{-5839.5}{T} - 22.4773\log(T) + 61.206 \tag{10}$$

$$\log(K_h) = \frac{818.55}{T} - 2.0957 \tag{11}$$

[a] Subscripts: 1−7 correspond respectively to $HCO_3^-$, $CO_3^{2-}$, $DEAH^+$, $DEACO_2^-$, $H^+$, $HO^-$, ETG. A: $CO_2$. B: DEA. I: inert ($N_2$). w: water.

sure in the installation around the set point. The gas flow leaving the setup, mainly inert nitrogen, is expanded to atmospheric pressure, and its volumetric flow rate is measured by means of a soap flowmeter.

**Physicochemical Properties and Thermodynamic Equilibria.** Nonidealities of the gas-phase ternary mixtures ($CO_2/N_2/H_2O_{vapor}$ or $ETG_{vapor}$) were taken into account using Peng and Robinson's equation of state (Reid et al., 1987). The viscosity of the gas mixture at high pressure was estimated according to Dean and Stiel's method (Reid et al., 1987). Diffusivity of $CO_2$ in the gas phase was estimated using Mathur and Thodos' correlation (Reid et al., 1987).

Some selected physicochemical properties of the amine solutions employed are listed in Table 2b. The viscosity and density of aqueous and organic DEA solutions were estimated from data reported by Versteeg et al. (1987), Versteeg and van Swaaij (1988), and Oyevaar et al. (1989). The same references provide data to estimate $CO_2$ and DEA diffusivities in the liquid solutions.

Activity coefficients of dissolved species in the liquid solutions were calculated from Pitzer's equation of state (Zemaitis et al., 1986). In aqueous DEA/ETG solutions, where $CO_2$ is absorbed, 10 species are formed or may be present: $CO_2$, $HCO_3^-$, $CO_3^{2-}$, DEA, $DEAH^+$, $DEACO_2^-$, $H^+$, $HO^-$, $H_2O$, ETG. Interactions between all these species were taken into account; details on the estimation of binary interaction coefficients can be found in Larachi (1991). The solvent activity was calculated following the approach of Edwards et al. (1978).

The liquid−vapor equilibrium for carbon dioxide is formally expressed by the following equation:

$$m_A^* = \frac{y_A^* P}{RT}\frac{\phi_A^*}{\gamma_A}\frac{\Lambda_0}{\rho_{sv}}\exp\left\{-\frac{v_A^\infty}{RT}(p - p_{sv})\right\} = C_{AG}^*\Pi \tag{1}$$

where the exponential factor accounts for the effect of pressure on the solubility (Krichevsky and Kasarnovsky, 1935). For the aqueous solutions, the partition coefficient $\Lambda_0$ of carbon dioxide in pure water at 298 K is equal to 0.86 (Edwards et al., 1978). At the same temperature in pure ETG, $\Lambda_0$ = 0.945 (Oyevaar et al., 1989). The activity coefficient $\gamma_A$ accounts for the salting out effect on carbon dioxide solubility due to the presence in the liquid phase of the above-mentioned species. The influence of salting out may be considerable for high absorption rates as the solution ionic strength increases strongly.

Besides liquid−vapor equilibrium, there are four more equilibria taking place into the solution: the instantaneous proton transfers for the acid/base equilibria of amine and of first and second acidity of carbonic acid, the water dissociation, and the carbamate hydrolysis. This last reaction needs to be accounted for because it is responsible for the formation of $CO_2$ in the liquid bulk via the *shuttle* mechanism (Danckwerts and Sharma, 1966). Table 3 gives the formal equations of these equilibria together with their temperature dependencies. The water dissociation constant and carbonic acid first and second acidity constants were taken from Edwards et al. (1978). The DEA basicity constant was taken from Blauwhoff and Bos (1981). The carbamate hydrolysis constant was estimated from Blauwhoff and van Swaaij (1980).

**Reaction Kinetics.** Reaction kinetics of $CO_2$ in DEA solutions has been exhaustively studied. Versteeg (1987) and Oyevaar et al. (1990) give comprehensive reviews and thorough information to evaluate the kinetic rate constants for different DEA concentrations in water/ETG solutions. There are several parallel reactions when $CO_2$ is absorbed into the solution: the amine carbamation and the acid−base/hydrolysis reactions of $CO_2$ (see Table 4). Carbamation proceeds through the formation of a *zwitterion* which reacts with the bases present in solution. The reaction partial order in carbon dioxide is 1, and the overall rate constant depends on DEA, water, hydroxyl, and bicarbonate concentrations. An overall reaction rate can be expressed as

$$r_{CO_2} = -\frac{d[CO_2]}{dt} = k_{ov}[CO_2] \tag{12}$$

**Table 4. Reactions Involved in the Absorption of $CO_2$ in DEA Solutions: Definitions of the Rate Constants Involved in the Overall Reaction Kinetics (eq 13)**

| reactions involved | kinetic constants involved in the overall reaction rate | | | | |
|---|---|---|---|---|---|
| $CO_2 + DEA \underset{k_{-1}}{\overset{k_2}{\longleftrightarrow}} DEA^+CO_2^-$ | $k_w$ ($s^{-1}$)[a] | $10^{329.85-110.54\ \log(T)-(17625.4/T)]}$ | | | |
| $DEA^+\ CO_2^- + DEA \xrightarrow{k_d} DEAH^+ + DEACO_2^-$ | $k^{\infty}_{OH^-}$[a] ($m^3 \cdot kmol^{-1} \cdot s^{-1}$) | $10^{[13.635-(2895/T)]}$ | | | |
| $DEA^+CO_2^- + OH^- \xrightarrow{k_o} H_2O + DEACO_2^-$ | b | 0% ETG | 20% ETG | 40% ETG | 100% ETG |
| $DEA^+CO_2^- \xrightarrow{k_h} H^+ + DEACO_2^-$ | $k_2$ ($m^3 \cdot kmol^{-1} \cdot s^{-1}$) | 7300 | 1350 | 1260 | 270 |
| $DEA^+CO_2^- + CO_3^{2-} \xrightarrow{k_c} HCO_3^- + DEACO_2^-$ | $k_2k_d/k_{-1}$ ($m^6 \cdot kmol^{-2} \cdot s^{-1}$) | 479 | 812 | 633 | 175 |
| $CO_2 + H_2O \xrightarrow{k_w} H^+ + HCO_3^-$ | $k_2k_h/k_{-1}$ ($m^6 \cdot kmol^{-2} \cdot s^{-1}$) | 3.7 | | | |
| $CO_2 + OH^- \xrightarrow{k_{OH^-}} HCO_3^-$ | $k_2k_h/k_{-1}$ ($m^6 \cdot kmol^{-2} \cdot s^{-1}$) | 85200 | | | |
| $k_{OH^-} = k^{\infty}_{OH^-}\dfrac{\gamma_A\gamma_6}{\gamma_1}$ (1, $HCO_3^-$; 6, $OH^-$) | $k_2k_c/k_{-1}$ ($m^6 \cdot kmol^{-2} \cdot s^{-1}$) | data at 60 °C available in Tseng et al. (1988) | | | |

[a] From Pinsent et al. (1956) and Danckwerts and Sharma (1966). [b] From Versteeg (1987) and Oyevaar et al. (1990).

where the overall rate constant is given by

$$k_{ov} = k_w + k_{OH^-}[OH^-] + \frac{[DEA]}{\dfrac{1}{k_2} + \dfrac{1}{\dfrac{k_2k_d}{k_{-1}}[DEA] + \dfrac{k_2k_h}{k_{-1}}[H_2O] + \dfrac{k_2k_0}{k_{-1}}[OH^-] + \dfrac{k_2k_c}{k_{-1}}[CO_3^{2-}]}} \tag{13}$$

The brackets [ ] indicate molar concentration in the liquid phase, and the different constants involved are defined in Table 4.

**Mass-Transfer Equations.** The specific transfer flux ($N_A$) of gaseous reactant A, i.e., carbon dioxide, absorbed into a liquid (the DEA solution), where it reacts following pseudo-first-order kinetics, can be expressed according to the penetration theory (Danckwerts, 1970) as

$$N_A = -\frac{G}{M_I}\frac{dY_A}{dz} = \frac{k_L a \rho_L x_{sv}\sqrt{1+Ha^2}}{1 + \dfrac{k_L}{k_G}\Pi\rho_L x_{sv}\sqrt{1+Ha^2}}\left[\Pi C_{AG} - \frac{m_A}{\sqrt{1+Ha^2}}\right] \tag{14}$$

where $N_A$ has also been expressed by the differential variation of the reactant concentration in the gas phase along the packed bed. Plug flow for the gas and the liquid has been assumed. Note that the gas mass velocity $G$ is based on inert nitrogen only. For other symbols appearing in eq 14, see the Nomenclature section.

*Determination of Interfacial Areas.* For high DEA concentration in aqueous solutions, chemical absorption of $CO_2$ is a suitable reaction to evaluate gas–liquid interfacial areas. Nonetheless, the four following conditions must be fulfilled:

(1) Gas-side mass-transfer resistance is negligible compared with the liquid-side resistance:

$$k_G \gg k_L\Pi\rho_L x_{sv}\sqrt{1+Ha^2} \tag{15}$$

This assumption is checked using values for the gas-side mass-transfer coefficient, $k_G$, estimated at atmospheric pressure by the correlation of Yaïci et al. (1988). As suggested by the penetration theory, the $k_G$ values are then correspondingly corrected for the decrease of carbon dioxide diffusivity with pressure. Increasing the pressure from 0.3 to 3.2 MPa decreases $k_G$ from $3.5 \times 10^{-2}$ to $0.6 \times 10^{-2}$ m/s for $L = 3.7$ kg/m$^2$·s and $G = 0.56$ kg/m$^2$·s. The liquid-side mass-transfer coefficient is estimated from Wild et al. (1992) atmospheric interfacial area and volumetric liquid-side mass-transfer coefficient correlations. The $k_L$ values estimated are in the range $1 \times 10^{-5}$–$8 \times 10^{-4}$ m/s which lead to $k_G/k_L = 7.5$–$3500$.

(2) Consumption of dissolved carbon dioxide should be fast to confine the chemical reaction within the liquid diffusional film nearby the interface:

$$Ha = \frac{\sqrt{k_{ov}D_{AL}}}{k_L} > 2 \tag{16}$$

The $k_L$ values estimated above correspond to $Ha$ numbers always larger than 6, thus fulfilling condition (16).

(3) DEA supply from the liquid bulk to the interface must be fast, i.e., negligible DEA depletion:

$$Ha < E_\infty = \sqrt{\frac{D_{AL}}{D_{BL}}} + \sqrt{\frac{D_{BL}}{D_{AL}}}\frac{m_B}{2m_A^*} \tag{17}$$

This conditions is always met for the DEA aqueous solutions. Enhancement factors under instantaneous reaction, $E_\infty$, are above 15.

(4) The reaction between DEA and carbon dioxide must be irreversible. Wammes et al. (1991) checked the reaction irreversibility using the absorption model derived by Versteeg et al. (1989) for his conditions of DEA concentrations, DEA conversions, and carbon dioxide conversion. As DEA–$CO_2$ conditions of the present work compare quite well with Wammes et al.'s (1991) conditions, irreversibility of the DEA carbamation reaction has been assumed.

Once the four conditions are satisfied, the transfer flux $N_A$ becomes independent of $k_L$ and eq 14 becomes (Danckwerts, 1970):

$$N_A = -\frac{G}{M_I}\frac{dY_A}{dz} = a\rho_L x_{sv}\sqrt{D_{AL}k_{ov}}\left[m_A^* - \frac{m_A}{Ha}\right] \tag{18}$$

Even knowing the inlet and outlet $CO_2$ mole ratios, it is not straightforward to obtain $a$ from eq 18 since $k_{ov}$, $m_A^*$, $m_A$, and $Ha$ vary as a function of the depth in the packed bed. The longitudinal profiles of $k_{ov}$, $m_A^*$,

**Table 5. Balance of Elements (N, H, C, $e^-$) for Aqueous DEA Solutions**[a]

$$m_B^i x_w^i = x_w(m_B + m_3 + m_4) \tag{19}$$

$$\left(m_B^i + \frac{2}{M_w}\right)x_w^i = x_w\left(m_B + m_1 + 2m_3 + m_5 + m_6 + \frac{2}{M_w}\right) + \frac{2G}{L}\frac{Y_I}{M_I} \tag{20}$$

$$\frac{G}{L}\frac{Y_A^i - Y_A}{M_I} = x_w(m_A + m_1 + m_2 + m_4) \tag{21}$$

$$m_3 + m_5 = m_1 + 2m_2 + m_4 + m_6 \tag{22}$$

[a] Subscripts: 1−7 correspond respectively to $HCO_3^-$, $CO_3^{2-}$, $DEAH^+$, $DEACO_2^-$, $H^+$, $HO^-$, ETG. A: $CO_2$. B: DEA. I: inert ($N_2$). w: water.

$m_A$, and *Ha* need to be computed by solving simultaneously the set of equations of equilibrium constants (Table 3) and elementary mass balance equations (Table 5). An iterative numerical procedure based on a combination of Newton−Raphson, Newton−Raphson with restriction on step size, Levenberg−Marquardt, and continuation methods has been used. Convergence of the above system of nonlinear algebraic equations was always fulfilled with residuals less than $10^{-4}$. Once the profiles are calculated, the interfacial area is obtained upon integration of eq 18 between reactor inlet and outlet $CO_2$ mole ratios.

*Determination of Volumetric Liquid-Side Mass-Transfer Coefficients.* For low DEA concentration in ETG solution, the chemical absorption of carbon dioxide is slow in the liquid diffusional film and fast in the liquid bulk to become a suitable model reaction for the evaluation of volumetric liquid-side mass-transfer coefficients, $k_La$. The following two conditions must, however, be verified:

(1) The amount of gas reactant diffusing through the liquid diffusional film far outweighs that consumed in the liquid diffusional film:

$$Ha = \frac{\sqrt{k_{ov}D_{AL}}}{k_L} < 0.3 \tag{23}$$

In the case of DEA/ETG solution, *Ha* values range between 0.014 and 0.065.

(2) The gas-phase mass-transfer resistance is negligible in comparison with the liquid-phase mass-transfer resistance:

$$k_G \gg k_L \Pi \rho_L x_{sv} \tag{24}$$

Once the two conditions are met, the transfer flux $N_A$ given by eq 14 simplifies to (Danckwerts, 1970)

$$N_A = -\frac{G}{M_I}\frac{dY_A}{dz} = k_L a \rho_L x_{sv}[m_A^* - m_A] \tag{25}$$

When the model equations from Tables 3 and 6are solved iteratively and eq 25 is integrated knowing inlet and outlet $CO_2$ mole ratios, $k_La$ values are obtained in a manner similar to that for interfacial areas (see above).

## Results and Discussion

**Gas−Liquid Interfacial Areas in TBR at High Pressure.** *Effect of Gas Density and Fluid Superficial Velocities.* Parts a and b of Figure 2 are plots of gas−liquid interfacial area and two-phase pressure drop as a function of gas superficial velocity. Different pressures and liquid superficial velocities were used. Due to the limited capacity of the gas cylinders, measurements could not be performed for gas superficial velocities in excess of 7 cm/s at 2.1 and 3.1 MPa. At a given pressure, the interfacial areas and the two-phase pressure drops exhibit the expected increase with gas and liquid velocities. Such trends coincide with those already reported for atmospheric conditions (Morsi et al., 1980; Midoux et al., 1984; Wild et al., 1992; Venkata Ratnam et al., 1994). For low liquid or gas superficial velocity ($u_L$ = 0.14 cm/s, $u_G \approx$ 2 cm/s), *a* weakly depends on pressure (Figure 2a). For liquid superficial velocities greater than 0.14 cm/s and gas superficial velocities above 2 cm/s, gas−liquid interfacial areas improve while pressure is increased. The increase of *a* with pressure is more pronounced for higher values of liquid superficial velocities. Figure 2b shows that the two-phase pressure drop also increases with pressure. From our previous studies, we also found that gas holdup is an

**Table 6. Balance of Elements (N, C, $e^-$) for ETG Solutions**[a]

$$m_B^i = m_B + m_3 + m_4 \tag{26}$$

$$\frac{G}{L}\frac{Y_A^i - Y_A}{M_I} = x_7^i m_4 \tag{27}$$

$$m_3 = m_4 \tag{28}$$

[a] Subscripts: 1−7 correspond respectively to $HCO_3^-$, $CO_3^{2-}$, $DEAH^+$, $DEACO_2^-$, $H^+$, $HO^-$, ETG. A: $CO_2$. B: DEA. I: inert ($N_2$). w: water.

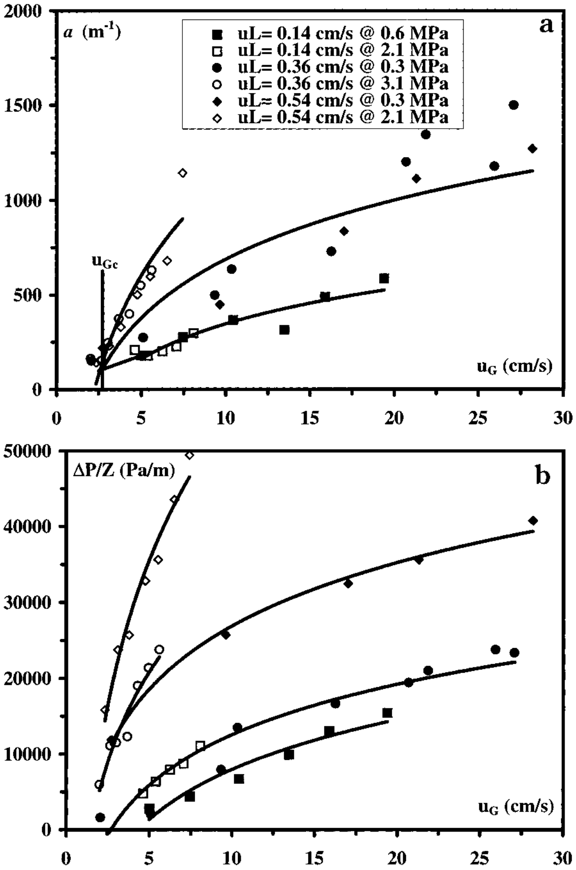

**Figure 2.** Effect of fluid velocities and pressure on (a) gas−liquid interfacial area and (b) two-phase pressure drop. System: water + 1.5 kmol/m$^3$ DEA/nitrogen, polypropylene extrudates. Curves show the trends.

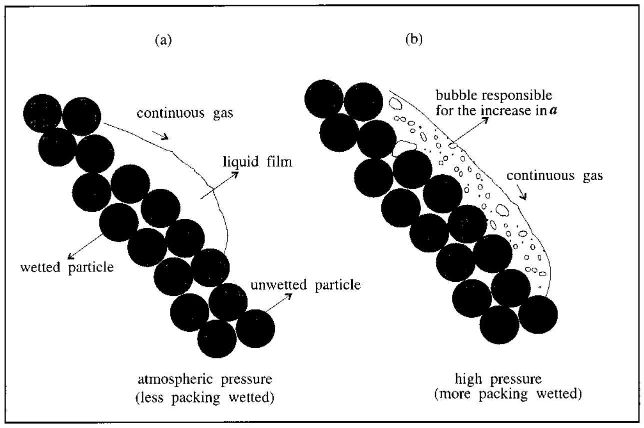

**Figure 3.** Sketch of the physical phenomenon responsible for gas–liquid interfacial mass-transfer enhancement due to elevated pressure: (a) atmospheric gas–liquid flow pattern; (b) high-pressure gas–liquid flow pattern.

increasing function of pressure (Larachi et al., 1994). Consequently, there is a clear indication that changes in gas–liquid interfacial area are interrelated to changes in gas holdup and two-phase pressure drop. It is worth mentioning that the volumetric liquid-side mass-transfer coefficient exhibits the same increase with pressure (Lara-Marquez et al., 1992).

*Model To Estimate the Increase of a due to Pressure in TBR.* In this section, a simple model is proposed to quantify the influence of pressure on gas–liquid interfacial areas. The model is based on the second viewpoint using pore-scale force arguments mentioned earlier to interpret the influence of pressure on TBR hydrodynamic parameters (see the Introduction section). For a given superficial gas velocity, gas shear over the trickling film intensifies while increasing pressure. The increase of gas–liquid interfacial shear impedes the gas–liquid interface from remaining smooth, and hydrodynamic instability at the gas–liquid interface causes entrainment of gas into the liquid. The entrained gas will disperse in the liquid film in the form of bubbles, thus increasing gas holdup and gas–liquid interfacial area. A phenomenological picture of this process is sketched in Figure 3. Schematically, in the low-pressure operation (close to 1 atm), the gas and the liquid may be viewed as totally segregated as gas-free liquid films sweeping the packing and a liquid-free continuous gas bulk occupying the complementary space in the porous medium. In the high-pressure operation, part of the gas mixes with the liquid to form gas–liquid film dispersion and the remaining gas lies as a liquid-free continuous gas bulk. The gas–liquid interfacial shear flattens and spreads the trickling films due to the action of increasing pressures, thereby enhancing wetting efficiency at high pressure. Evidence of the increase of wetting efficiency with pressure was experimentally verified in the recent works of Al-Dahhan and Duduković (1995, 1996). Consequently under high-pressure conditions, the global gas–liquid interfacial area may be split into a macroscopic surface area and a microscopic surface area. The macroscopic surface area is the boundary between the liquid-free gas bulk and the film (Figure 3a), and the microscopic surface area is the boundary between the bubbles and the liquid within the film (Figure 3b).

The size of bubbles present in the film is considered to be governed by two opposite forces, the liquid viscous shear stress, which tends to deform and break the bubbles up, and the force induced by interfacial tension, which tends to stabilize them. To quantify the net effect, a mean bubble diameter has to be estimated. For this purpose, Taylor's theory (Taylor, 1934; Hinze, 1955) has been used with the subsequent refinements brought to the theory for bubble deformation and breakup in sheared emulsions (Torza et al., 1972; Bentley and Leal, 1986; Utracki and Shi, 1992). According to Taylor (1934), the bubble size in a sheared emulsion is an outcome of a balance between the viscous and surface tension forces. The dimensionless number that relates these forces is usually called the capillarity number. The maximum stable bubble diameter in a shear flow may be obtained from the following expression:

$$\Omega_c = \frac{\tau d_{\mathrm{Max}}}{\sigma_L} = C \tag{29}$$

where $\tau$ is the viscous shear stress exerted by the gas–liquid emulsion on the bubbles and is given by the product of the effective emulsion viscosity and the maximum liquid velocity gradient; $d_{\mathrm{Max}}$ is the diameter of the largest bubble that can withstand the external forces; and $\Omega_c$ is the critical capillarity number which corresponds to the condition at bubble burst and can be fitted from experimental data.

Since the ratio of dispersed to continuous phase viscosities, $\lambda$, considerably affects the bubble stability, Bentley and Leal (1986) suggested a theory for large bubble deformations to estimate $\Omega_c$. This theory is valid for $\lambda \le 0.02$, i.e., where the critical capillarity numbers are large and depend upon the viscosity ratio. According to this theory:

$$\Omega_c = \frac{\tau d_{\mathrm{Max}}}{\sigma_L} = C\lambda^{-1/6} \tag{30}$$

Parent bubbles generally breakup into daughter bubbles of similar sizes and produce some very small satellite bubbles. The number of satellite bubbles depends on the way the liquid gradient is established. If the rate of increase in liquid gradient until the one that produces the bubble breakup is small, only a few satellite bubbles are produced (Torza et al., 1972). Moreover, for low viscosity ratios ($\lambda \le 0.02$), bubbles deform as spheroids with pointed ends from which only small microbubbles are ejected. This type of bubble erosion is known as the *tip spinning* mechanism (Utracki and Shi, 1992).

To apply this model to our work, the following assumptions have been made on the bubble Sauter diameter to describe the gas–liquid mass-transfer phenomenon:

(i) The model applies to gas–liquid mass transfer in the trickle flow regime under fully or partially wetted conditions of the packing.

(ii) Contribution to gas holdup and gas–liquid interfacial area of very small satellite bubbles formed during breakup is negligible. Only relatively large bubbles (between 0.1 and 1 mm) are considered.

(iii) A constant ratio between the bubble Sauter diameter and the maximum bubble diameter is assumed: $d_S \cong \alpha d_{\mathrm{Max}}$.

(iv) Bubble Sauter diameter is defined as

$$d_S = \frac{6\epsilon\beta_b}{a_b} = \frac{6(\beta_L^\circ - \beta_L)\epsilon}{(a - a^\circ f/f^\circ)} \tag{31}$$

where $\epsilon\beta_b$ and $a_b$ are respectively the gas holdup (expressed per unit reactor volume) and the gas–liquid interfacial area (expressed per unit reactor volume) of the bubbles present in the film (Figure 3b). It is postulated that bubbles do not exist at atmospheric pressure in the trickle flow regime. At elevated pressure, $\epsilon\beta_b$ and $a_b$ may be evaluated from a balance between the actual values of liquid holdup and interfacial area (respectively $\epsilon\beta_L$ and $a$) and those corresponding to atmospheric pressure (respectively $\epsilon\beta_L^\circ$ and $a^\circ$), as expressed in eq 31. The increase in $a$ due to the larger liquid spreading expected at high pressure (Al-Dahhan and Duduković, 1995, 1996) is accounted for by introducing the ratio of wetting efficiencies at high pressure ($f$) and at 1 atm ($f^\circ$).

(v) As the viscosity of the film may be affected by the presence of bubbles, the gas–liquid emulsion is assumed to remain Newtonian and its effective viscosity is estimated according to Einstein's equation (see Barnes et al., 1989):

$$\mu_L^* = \mu_L\left(1 + 2.5\frac{\beta_b}{\beta_b + \beta_L}\right) = \mu_L\left(1 + 2.5\left(1 - \frac{\beta_L}{\beta_L^\circ}\right)\right) \qquad (32)$$

The coefficient 2.5 in eq 32 is valid for emulsions of rigid spheres. For an emulsion of small gas bubbles, the value of this coefficient lies between 1 and 2.5 and depends on the viscosity ratio $\lambda$. For the sake of simplicity, a value of 2.5 is assumed.

Substituting $d_S$ from eq 31 into eq 33 and assuming that the shear stress in the liquid is $\tau = \mu_L^*(u_L/\epsilon\beta_L)/\delta_L$, the following equation is obtained:

$$\frac{6(\beta_L^\circ - \beta_L)\epsilon}{(a - a^\circ f/f^\circ)\alpha\sigma_L}\left(\mu_L^*\frac{u_L/\epsilon\beta_L}{\delta_L}\right) = C\lambda^{-1/6} \qquad (33)$$

In eq 33, the liquid velocity gradient is written as the ratio between the interstitial liquid velocity and the film thickness, $\delta_L$. Finally, taking $\kappa = 6/\alpha C$ and rearranging, eq 33 becomes

$$a = a^\circ\frac{f}{f^\circ} + \kappa Ca\frac{\lambda^{1/6}}{\delta_L}\left(\frac{\beta_L^\circ}{\beta_L} - 1\right)\left(1 + 2.5\left(1 - \frac{\beta_L}{\beta_L^\circ}\right)\right) \qquad (34)$$

where $Ca$ is the capillarity dimensionless ratio.

Equation 34 contains two terms: the first term designates the macroscopic interfacial area which consists of the interface between the bulk gas and the two-phase emulsion at high pressure corrected for the film spreading, whereas the second term represents the microscopic interfacial area due to the bubble–liquid interface inside the film (Figure 3b).

The film thickness, $\delta_L$, at high pressure is calculated as the ratio between the film volume and the macroscopic interfacial area at high pressure:

$$\delta_L = \frac{\epsilon(\beta_L + \beta_b)}{a^\circ f/f^\circ} = \frac{\epsilon\beta_L^\circ}{a^\circ f/f^\circ} \qquad (35)$$

Replacing $\delta_L$ in eq 34 results in the following:

$$a = a^\circ\frac{f}{f^\circ}\left\{1 + \kappa\left(\frac{\mu_G}{\mu_L}\right)^{1/6}\frac{Ca}{\epsilon}\left(1 + 2.5\left(1 - \frac{\beta_L}{\beta_L^\circ}\right)\right)\left(\frac{1}{\beta_L} - \frac{1}{\beta_L^\circ}\right)\right\} \qquad (36)$$

Equation 36 is a model with one single fitted parameter and allows estimation of gas–liquid interfacial areas at high pressure provided that liquid holdup, $\beta_L$, and wetting efficiency, $f$, are known under the same conditions. To calculate $a$ from eq 36, $\beta_L^\circ$ $a^\circ$, and $f^\circ$ at 1 atm are also required. These can be measured, if possible, or estimated from correlations. Liquid holdups at 1 atm and at high pressure were estimated from the correlation of Larachi et al. (1991). Wetting efficiencies at 1 atm and at high pressure were estimated using the correlation of Al-Dahhan and Duduković (1995). For interfacial area at 1 atm, the transition correlation of Wild et al. (1992) was used. As will be discussed later, this is the only correlation which provided the more accurate description of interfacial areas.

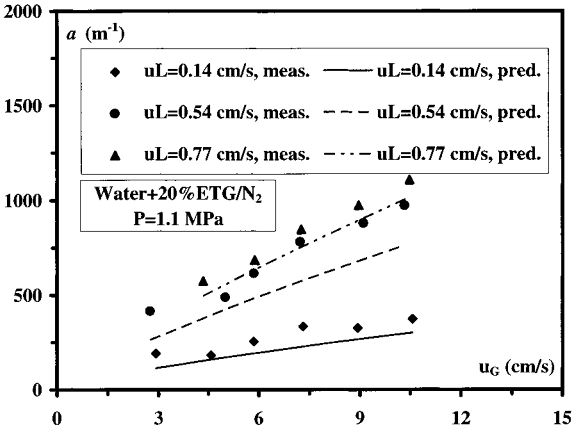

**Figure 4.** Trend of the present model (q 36) prediction versus measurement of gas–liquid interfacial areas as a function of gas and liquid superficial velocities and constant pressure.

Equation 36 is valid only if the liquid film is of sufficient thickness to host the bubbles formed; i.e., if $\delta_S < \delta_L$. Physically, this condition is fulfilled if

$$\frac{6\beta_L\epsilon\left(\frac{\mu_L}{\mu_G}\right)^{1/6}}{\kappa Ca\left(1 + 2.5\left(1 - \frac{\beta_L}{\beta_L^\circ}\right)\right)} < 1 \qquad (37)$$

Inequality (37) provides an objective criterion to decide whether or not pressure effects on $a$ should be taken into account. The numerical constant, $\kappa$, is obtained from the present data and data of Wammes et al. (1991) that fulfill inequality (37). The best estimate is found to be $\kappa = 2.65 \times 10^4$.

*Comparison of the Model and the High-Pressure Interfacial Areas.* Figure 4 compares model predictions to experimental interfacial areas when only gas and liquid superficial velocities vary while the pressure is held constant. As shown in Figure 4 and in agreement with experimental observations, the model predicts interfacial areas increasing with both fluid velocities.

Model prediction of the effect of pressure on gas–liquid interfacial areas is compared to data of this work and data of Wammes et al. (1991) in Figure 5a,b, respectively. Here too, agreement is somewhat accurate. For the highest gas superficial velocity in Figure 5b, the divergence in the model prediction becomes significant particularly at high liquid mass fluxes. It is well-known that the chemical methods intrinsically fail to capture the true geometrical interfacial areas for high conversion of the gaseous reactant. This is likely to occur at high gas and liquid throughputs where the chemical interfacial area is less than the geometrical

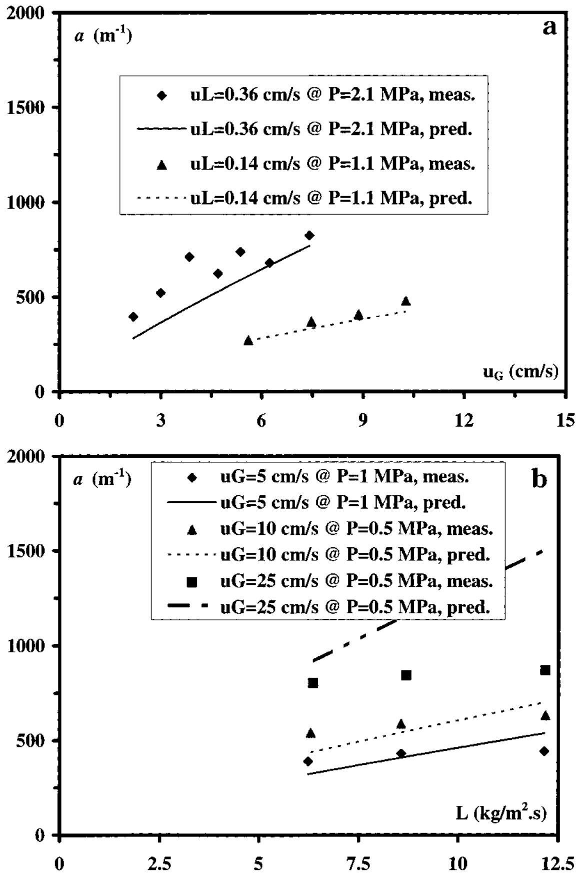

**Figure 5.** Trend of the present model (eq 36) prediction versus measurement of gas–liquid interfacial areas as a function of gas and liquid superficial velocities and varying pressures: (a) data of this work; (b) Wammes et al. (1991) data.

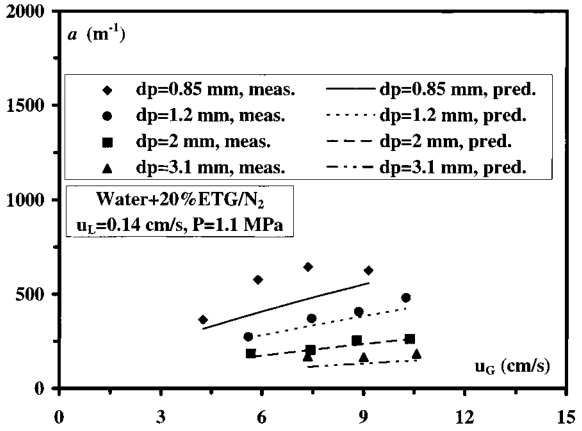

**Figure 6.** Trend of the present model (eq 36) prediction versus measurement of gas–liquid interfacial areas as a function of gas superficial velocity and varying packing dimensions.

interfacial area. Therefore, measurements in these conditions are less accurate and do not allow an objective assessment of the model performances.

Gas–liquid interfacial areas have also been measured under high-pressure conditions using packings of different size, shape, and material. Some sample results are shown in Figure 6. For particles of the same material and shape (glass beads of different diameters), the gas–liquid interfacial area increases as the particle diameter decreases. This trend is clearly observed at low liquid velocities and is coincident with the behavior at atmospheric conditions. Once more, values predicted by eq 36 provide satisfactory estimations.

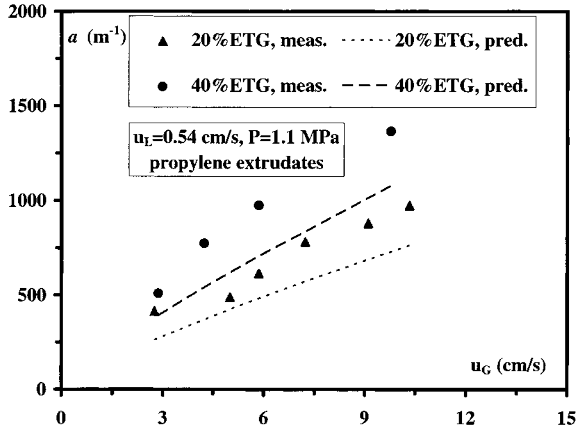

**Figure 7.** Trend of the present model (eq 36) prediction versus measurement of gas–liquid interfacial areas as a function of gas superficial velocity and varying liquid viscosities.

While comparing particles of the same size but of different shapes (glass beads and polypropylene extrudates) or porous and nonporous particles (glass beads, porous activated carbon, or alumina spheres), it was found that the nonspherical and porous particles generate the largest interfacial areas. Such packing geometry features are more evident at low liquid velocities and fade, but still exist, for higher liquid velocities.

The influence of liquid viscosity on gas–liquid interfacial areas is shown in Figure 7, where *a*-values are plotted versus gas superficial velocity for the less and the most viscous of the three solutions studied in this work. Predictions of eq 36 are also shown. An increase in liquid viscosity induces an increase in gas–liquid interfacial area in the same manner as at atmospheric pressure (Morsi et al., 1980, 1984). Although the model qualitatively captures the liquid viscosity feature, it underestimates the measured values. The prediction error is bounded by the −60% limit. Wammes et al. (1991) also reported that, by increasing liquid viscosity, gas–liquid interfacial areas improve. However, even if comparable liquid viscosity ratios were used in the two studies, we do not measure comparable changes in interfacial areas. In our opinion this can be ascribed to liquid foaminess which differed in the two studies. While in the present work we strove to use only fresh, noncontaminated DEA solutions, Wammes et al. (1991) used regenerated DEA solutions in which trace amounts of impurities might be responsible for deep modifications of interfacial characteristics.

*Prediction of Bubble Size and Film Thickness.* Rigorously to validate the above two-zone model, it is necessary to have an independent experimental verification of the existence of such bubbles in the trickling films that would explain mass-transfer enhancement due to increased pressure. A flow visualization technique would likely be the most suited method. At present, implementation of such a technique is yet not possible for a trickle bed operated at high pressure for which physical constraints such as thick-walled or nontransparent columns impede easy observations. An indirect means to assess the validity of the proposed approach will be to simulate the bubble behavior and to judge whether the trends predicted are realistic and similar to bubble behavior expected from analogies with other types of gas–liquid or gas–liquid-solid reactors. This is the purpose of this section.

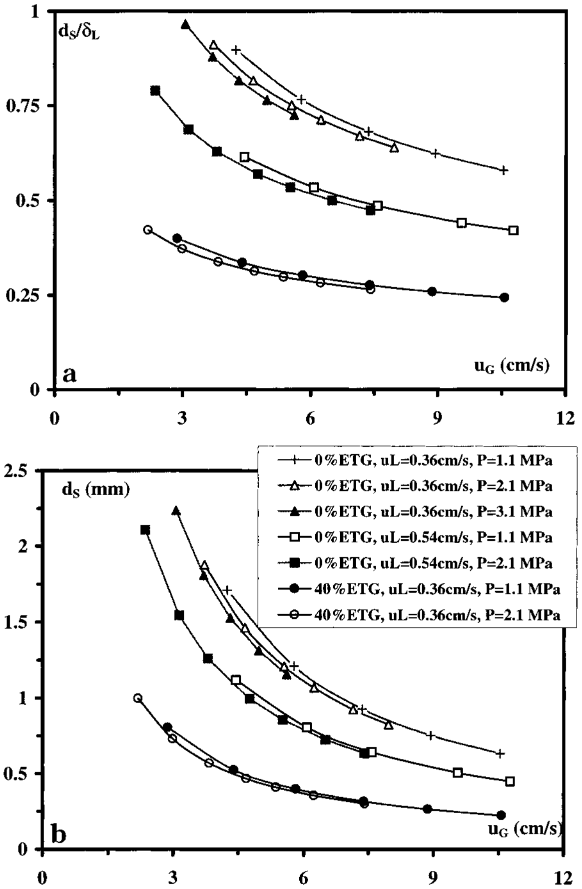

**Figure 8.** Simulation of (a) bubble Sauter diameter-to-liquid film thickness ratio and (b) bubble Sauter diameter as a function of pressure, liquid and gas superficial velocities, and liquid viscosities using the present model. Curves are simulations from eqs 31, 35, and 36, and symbols refer to the pressure and the solutions used.

Variations in gas and liquid velocities, pressure, and liquid viscosity on the bubble Sauter diameter (eq 31) and film thickness (eq 35) are simulated using the model (eq 36) within the experimental range investigated here. Parts a and b of Figure 8 show respectively simulations of $d_S/\delta_L$ and $d_S$ ratios as a function of gas velocity at two liquid velocities, three pressures, and two liquid viscosities. Data shown in Figure 8a obey inequality (37). Recall that this inequality results from geometrical considerations. The formation and existence of stable bubbles in the film is precluded for $d_S/\delta_L > 1$, that is, if inequality (37) is violated. Moreover and as expected, at given pressure and fluids system, the model (eqs 31 and 36) predicts a bubble size decreasing with increasing gas and/or liquid superficial velocities (Figure 8b). Due to a larger viscous shear stress, bubbles at $u_L = 0.54$ cm/s are smaller than those at $u_L = 0.36$ cm/s. For given gas and liquid superficial velocities, when pressure is increased from 1.1 to 3.1 MPa, bubbles get slightly smaller but more bubbles are entrained in the film ($\epsilon\beta_b$ increasing with pressure) in order that the microscopic interfacial area gets larger. The influence of pressure on the microscopic interfacial area is more pronounced with low-viscosity liquids compared with high-viscosity liquids. This is shown by the 3-times smaller bubbles prevailing with the 3.8 mPa·s 40% ETG solution than with the 1.2 mPa·s ETG-free solution (Figure 8b). It has to be mentioned that similar viscosity effects have also been reported for gas holdups and interfacial areas in sparged reactors such as bubble columns or three-phase fluidized beds (see works summarized in Table 1).

*Comparison of the Present Model and Available Interfacial Area Correlations.* The high-pressure gas–liquid interfacial areas obtained in this study together with data formerly measured by Wammes et al. (1991) are used as a basis for performing statistical tests of the proposed model and the available interfacial area correlations. To our knowledge, the data reported in this study on high-pressure interfacial areas in TBRs are the only data existing in the open literature. Furthermore, only the literature correlations developed for the trickle flow regime or for the transition between trickle and pulse flow regimes are considered in our analysis. It should be emphasized that all these correlations are empirical in nature and almost all are exclusively derived based on atmospheric mass-transfer data. A statistical comparison in terms of mean relative error (average of the relative absolute difference between the measured and the predicted values divided by the measured value) is given in Table 7. Except for the Midoux et al. (1984) correlation, most of the tested correlations were highly biased and either underpredicted or overpredicted present interfacial area measurements. Clearly, it is our model that describes high-pressure data the most accurately. This can be explained by the physical grounds on which the proposed model is established in opposition to the empirically derived correlations. Despite that our model requires fitting one parameter ($\kappa$), it proposes a physical interpretation of how pressure affects gas–liquid interfacial areas. Besides, parameter $\kappa$ has a physical meaning; it is a function of the bubble size distribution and the critical capillarity number. The prediction error of the proposed model for all the interfacial area data at high pressure is encompassed within ±60% limits, as is shown in Figure 9. However, as can be seen from the figure, a few high values of measured interfacial areas are underpredicted by the model and escape from the −60% bound. Close examination of those data reveals that they were obtained in a bed of $d_c/d_p \approx 8$ and for the lowest pressure level tested in our work (0.3 MPa). Such a low column-to-particle diameter ratio is suspected to alter somewhat the interfacial area due to liquid maldistribution and wall channeling. Moreover, for the lowest pressure the interfacial areas were obtained close at the transition between trickle and pulse flow regime, where we suspect foaming of diethanolamine solutions is no longer negligible.

**Volumetric Liquid-Side Mass-Transfer Coefficient in TBR at High Pressure.** Volumetric liquid-side mass-transfer coefficients, $k_La$, at high pressure were also measured. As for $a$, the effect of pressure on $k_La$ is felt only beyond critical values of gas and liquid velocities. As shown in Figure 10, $k_La$ increases while increasing the pressure for gas superficial velocity above 2 cm/s. The pressure dependency of $k_La$ may be the result of variations of (i) the interfacial area alone, (ii) the liquid-side mass-transfer coefficient $k_L$ alone, or (iii) both $k_L$ and $a$. Variations of $k_La$ via $a$ while working at high pressure have been clearly identified in the previous section of the present work. Moreover, based on data of the above literature survey, mass-transfer coefficient $k_L$ at high pressure in various gas–liquid and gas–liquid–solid contactors is unlikely to change with pressure in the common range of pressures up to a few megapascals. Therefore, it is claimed that $k_La$ varies

**Table 7. Comparison of Some Literature Interfacial Area Correlations to Data[a] in High-Pressure TBRs in Terms of Mean Relative Error[b]**

| ref (eq no.) | correlation[c] | $\hat{e}$ (%) | remark[d] |
|---|---|---|---|
| Hirose et al., 1974 (38) | $a = 175\ d_p^{-0.8} u_G^{0.6} u_L^{0.5}$ | 47 | U (−80%) |
| Charpentier, 1976 (39) | $a = 0.05 a_c \left(\frac{\Delta P}{Z} \frac{\epsilon}{a_c}\right)^{0.5}$ | 66 | U (−100%) |
| Fukushima and Kusaka, 1977 (40) | $a = 0.0039 \frac{(1 - \beta_L)}{d_p} Re_L^{0.4} \left(\frac{d_p}{d_c}\right)^{-2} (\varphi)^{-0.1}$ | 94 | U (−100%) |
| Bakos et al., 1980 (41) | $a = 0.35 a_c \left(\frac{\epsilon}{a_c}\left(\frac{\Delta P}{Z}\right)\right)^{0.55}$ | 205 | O (400%) |
| Morsi, 1989 (42) | $a = 0.66\left(\frac{\Delta P}{Z} + \epsilon g[\beta_L \rho_L + (1 - \beta_L)\rho_G]\right)^{0.65}$ | 51 | U (−80%) |
| Midoux et al., 1984 (43) | $a = 1.47 \times 10^5 \epsilon \left(\frac{\epsilon^2 \xi_{LG}}{a_c\left(\frac{L}{\rho_L} + \frac{G}{\rho_G}\right)}\right)^{0.65}$ | 52 | ±100% |
| Wild et al., 1992 (low interaction, 44) | $a = 10 a_c \left(X_G Re_L^{-0.5} We_L \left(\frac{\mathrm{a}_c d_K}{1 - \epsilon}\right)^{1.5}\right)^{0.7}$ | 55 | U (−80%) |
| Wild et al., 1992 (transition, 45) | $a = 21.3 a_c \left(X_G Re_L^{-0.5} We_L \left(\frac{a_c d_K}{1 - \epsilon}\right)^{-2}\right)^{0.5}$ | 44 | U (−80%) |
| Venkata Ratnam and Varma, 1991 (46) | $a = 17.0 u_L^{0.30} \epsilon^{-1.20} d_e^{-0.50}$ | 56 | U (−100%) |
| Venkata Ratnam et al., 1994 (47) | $a = 375\left[\frac{g \mu_L^4}{\rho_L \sigma^3}\right]^{0.05} \epsilon^{1.40} \left[\frac{\Delta P}{Z} \frac{u_L}{\epsilon}\right]^{0.40}$ | 49 | U (−100%) |
| this work (36) | $a = a^\circ \frac{f}{f^\circ}\left\{1 + \kappa\left(\frac{\mu_G}{\mu_L}\right)^{1/6} \frac{Ca}{\epsilon}\left(1 + 2.5\left(1 - \frac{\beta_L}{\beta_L^\circ}\right)\right)\left(\frac{1}{\beta_L} - \frac{1}{\beta_L^\circ}\right)\right\}$ | 35 | ±60% |

[a] Including our data and Wammes et al. (1991) data. [b] U = underpredicted. O = overprotected. [c] Dimensional correlations in SI units. [d] $\hat{e} = 100(1/n)\sum_1^n |1 - a(\text{predicted})/a(\text{measured})|$. $n$ = number of data.

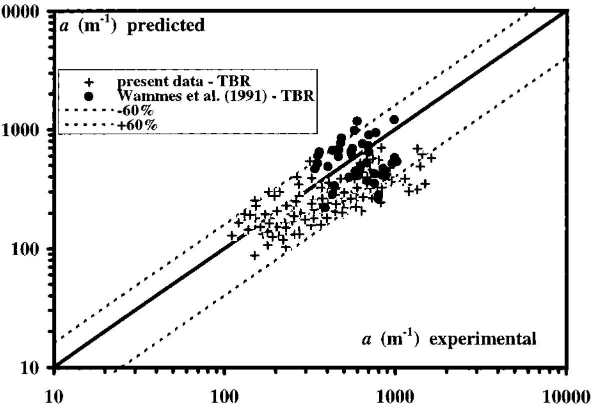

**Figure 9.** Parity plot comparing eq 36 predictions and high-pressure interfacial areas of the present work and of Wammes et al. (1991).

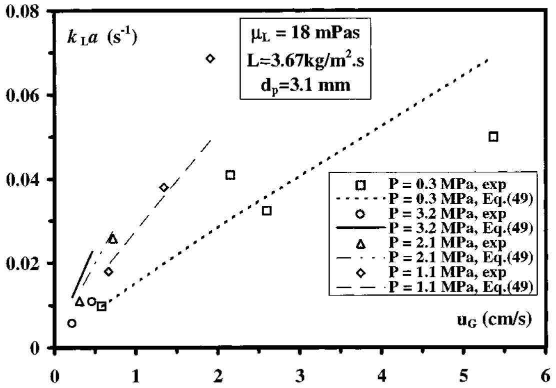

**Figure 10.** Effect of gas velocity and pressure on the volumetric liquid-side mass-transfer coefficient. System: ETG + 0.05 kmol/m$^3$ DEA/nitrogen, polypropylene extrudates. Lines represent model predictions using eq 49.

with pressure by the exclusive change of interfacial area with pressure.

Following the above two-zone model and by analogy with interfacial area, $k_L a$ may be separated into (i) a mass transfer from the continuous gas bulk to the trickling film with a mass-transfer coefficient akin to the one at 1 atm but corrected for partially wetted packing and (ii) a mass transfer from the bubbles to the surrounding liquid of the film, as if bubbles were suspended in a stagnant medium. The last assumption is made considering that the tiny bubbles travel sliplessly within the film. For illustration Figure 3 may be consulted.

The volumetric liquid-side mass-transfer coefficient at atmospheric pressure is estimated from the Wild et al. (1992) transition correlation. Then, contribution of mass transfer due to the bubbles is calculated as the product of the excess interfacial area $a_b$ and the mass-transfer coefficient of a bubble surrounded by an infinite stagnant medium, i.e., $Sh = k_L d_S / D = 2$:

$$k_L a = (k_L a)^\circ \frac{f}{f^\circ} + k_L^{(Sh=2)} a_b \tag{48}$$

Using eqs 31 and 36 and after rearranging, one obtains

$$k_L a = a^\circ \frac{f}{f^\circ}\left\{k_L^\circ + \frac{\kappa^2 D}{3\epsilon^3}\left(\frac{\mu_G}{\mu_L}\right)^{1/3}\left(a^\circ \frac{f}{f^\circ}\right)\frac{Ca^2}{\beta_L \beta_L^\circ}\left(\frac{1}{\beta_L} - \frac{1}{\beta_L^\circ}\right)\left(1 + 2.5\left(1 - \frac{\beta_L}{\beta_L^\circ}\right)\right)^2\right\} \tag{49}$$

$k_L a$ values predicted from eq 49 and measured with the ETG/DEA system are confronted in Figure 10 and in the parity plot of Figure 11. Equation 49 provides reasonable estimates of the volumetric liquid-side mass-

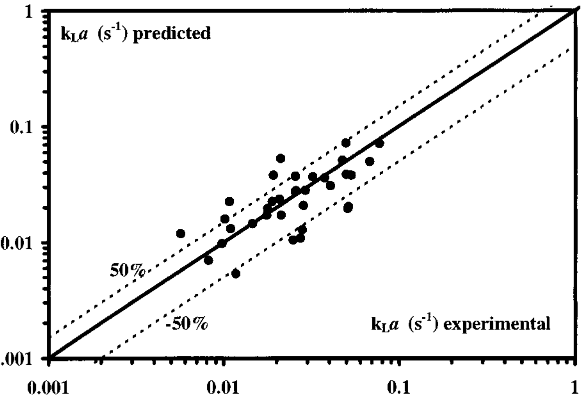

**Figure 11.** Parity plot comparing eq 48 predictions and high-pressure volumetric liquid-side mass-transfer coefficient of the present work.

transfer coefficients at high pressure. It is worth noting that eq 49 is derived using the parameter $\kappa$ fitted with the interfacial area data and not with the $k_La$ data of the ETG/DEA system.

## Concluding Remarks

Gas-liquid interfacial areas and volumetric liquid-side mass-transfer coefficients in trickle-bed reactors improve in the trickle flow with an increase in pressure at the expense of increased pressure drops and gas holdups. In the trickle flow regime, gas–liquid interfacial areas increase with increasing liquid viscosity. For identical equivalent diameters, spherical and nonporous particles give the lowest interfacial areas.

Qualitatively, improvement of gas–liquid mass transfer with pressure in the trickle flow regime is explained by postulating a two-zone flow pattern: (i) a liquid-free gas continuous phase and (ii) a gas–liquid film emulsion flowing down the packing, thereby creating (i) a macroscopic gas–liquid interfacial area and (ii) a microscopic gas–liquid interfacial area. The microscopic interface is composed of tiny bubbles which form in the films due to intensification of gas–liquid interfacial stress with pressure. The macroscopic interface is the boundary between the trickling film and the liquid-free continuous gas bulk.

Quantitatively, Taylor's theory of fluid–fluid sheared emulsions is used to relate the bubble size and the bubble holdup to the increase of interfacial area and gas holdup with pressure. A bubble Sauter diameter in the film is defined and related to viscous shear stress and surface tension force, the two competing forces that determine the bubble size. The two-zone model derived accounts satisfactorily well for the whole up-to-date high-pressure interfacial area data. The model is also extended to estimate the volumetric gas–liquid mass-transfer coefficient in high-pressure TBRs.

Finally, the present work is not intended with the ambition to be used for scaling up gas–liquid interfacial mass transfer to large-scale and hot trickle-bed reactors of 3–10 feet diameters and 30–100 ft heights. Being mostly based on experimental information obtained in small-scale laboratory columns, it is rather a contribution that will help us gain a better understanding of the complex phenomena taking place in TBRs. For the foreseeable future and as long as new reactor design paradigms are not elaborated, the design and scaleup of trickle beds will continue to be a matter of know how and rules of thumb.

## Acknowledgment

The authors gratefully acknowledge the financial support of the Institut Français du Pétrole (Solaize, France), the Algerian Ministry of Education, and Laval University. M.C. acknowledges comments of Dr. N. O. Lemcoff and financial support from University of Buenos Aires. Financial help of NSERC and FCAR is also acknowledged.

## Nomenclature

$A_p$ = particle external surface area ($m^2$)
$a$ = gas–liquid interfacial area per unit reactor volume ($m^{-1}$)
$a_c$ = external area of the particles per unit reactor volume ($m^{-1}$)
$C$ = molar concentration ($kmol/m^3$)
$Ca$ = capillarity dimensionless ratio, $Ca = u_L\mu_L/\sigma_L$
$D$ = diffusion coefficient in the liquid phase ($m^2/s$)
$d_{Max}$ = maximum bubble diameter (m)
$d_S$ = bubble Sauter diameter, $D_S = 6\epsilon\beta_b/a_b$ (m)
$d$ = diameter (m)
$d_c$ = column diameter (m)
$d_e$ = equivalent diameter, $6V_p/A_p$ (m)
$d_K$ = Krischer–Kast hydraulic diameter, $d_K = d_p[16\epsilon^3/9\pi(1-\epsilon)^2]^{1/3}$ (m)
$E_\infty$ = enhancement factor for absorption with an infinitely fast chemical reaction
$\hat{e}$ = mean relative error
$f$ = wetting efficiency
$G$ = gas mass velocity ($kg/m^2{\cdot}s$)
$g$ = gravitational acceleration ($m/s^2$)
$Ha$ = Hatta number, $Ha = (D_Ak_{ov})^{1/2}/k_L$
$K_b$, $K_{c1}$, $K_{c2}$, $K_w$, $K_h$ = equilibrium constants defined in Table 3
$k_G$ = gas-side mass-transfer coefficient (m/s)
$k_L$ = liquid-side mass-transfer coefficient (m/s)
$k_{ov}$ = overall kinetic constant defined in eq 13 ($s^{-1}$)
$k_2$, $k_{-1}$, $k_d$, $k_o$, $k_h$, $k_i$, $k_w$, $k_{OH^-}$ = kinetic constants involved in $k_{ov}$, defined in Table 4
$L$ = liquid mass velocity ($kg/m^2{\cdot}s$)
$M$ = molecular weight (kg/kmol)
$m$ = molality (kmol/kg)
$N$ = molar gas–liquid mass-transfer flux ($kmol/m^2{\cdot}s$)
$p$ = partial pressure (Pa)
$p_{sv}$ = solvent vapor pressure (Pa)
$P$ = operating pressure (Pa)
$R$ = universal gas constant (J/kmol·K)
$Re$ = Reynolds number, $Re = Ld_e/\mu$
$r$ = reaction rate ($kmol/m^3{\cdot}s$)
$Sh$ = Sherwood number, $Sh = k_Ld_b/D$
$T$ = temperature (K)
$t$ = time (s)
$u$ = superficial velocity (m/s)
$V$ = volume ($m^3$)
$V_p$ = volume of particle ($m^3$)
$v^\infty$ = molal volume at infinite dilution in the liquid solvent ($m^3/kmol$)
$We$ = Weber number, $We = L^2d_e/\rho\sigma$
$x$ = mole fraction in the liquid phase
$X_G$ = modified Lockhart–Martinelli ratio, $X_G = (G/L)(\rho_L/\rho_G)^{1/2}$
$Y$ = mole ratio in the gas phase, defined over the moles of inert
$y$ = mole fraction in the gas phase
$z$ = axial position

### *Greek Symbols*

$\alpha$ = ratio of bubble Sauter diameter to maximum bubble diameter, assumed constant
$\beta$ = holdup defined as a fraction of porous volume

$\delta$ = film thickness (m)
$\Delta P/Z$ = pressure drop (Pa/m)
$\epsilon$ = bed porosity
$\phi$ = fugacity coefficient
$\gamma$ = activity coefficient
$\kappa$ = numerical constant
$\Lambda_0$ = partition coefficient
$\lambda$ = viscosity ratio, $\lambda = \mu_G/\mu_L$
$\varphi$ = dimensionless factor that appears in Fukushima–Kusaka correlation, Table 7, $\varphi = A_p/d_p^2$
$\mu$ = viscosity (Pa·s)
$\mu^*$ = effective emulsion viscosity (Pa·s)
$\Omega_c$ = critical capillarity number defined in eqs 29 and 30
$\Pi$ = partition coefficient ($m^3$/kg)
$\rho$ = density (kg/$m^3$)
$\sigma$ = surface tension (N/m)
$\tau$ = viscous shear stress acting on the bubbles (N/$m^2$)
$\xi_{LG}$ = power dissipation rate,

$$\frac{u_L + u_G}{\epsilon g \rho_w}\frac{\Delta P}{Z} + \frac{\rho_L u_L}{\epsilon \rho_w} + \frac{\rho_G u_G}{\epsilon \rho_w}$$

(m/s)

*Subscripts*

A = $CO_2$ (gaseous reactant)
B = DEA (liquid reactant)
b = bubbles in the liquid film
c = critical
G = gas
I = inert
L = liquid
p = particle
w = water

*Superscripts*

° = at atmospheric pressure
* = relative to the interface or at equilibrium
i = corresponding to the inlet concentration

*Acronyms*

AC = autoclave
AR = agitated reactor
ASR = agitated slurry reactor
BC = bubble column
DEA = diethanolamine
ETG = ethylene glycol
FBR = flooded-bed reactor
GL = gas–liquid
GLS = gas–liquid–solid
TBR = trickle-bed reactor
VOC = volatile organic compound

## Literature Cited

Albal, R. S.; Shah, Y. T.; Schumpe, A.; Carr, N. L. Mass Transfer in Multiphase Agitated Contactors. *Chem. Eng. J.* **1983**, *27*, 61.

Albal, R. S.; Shah, Y. T.; Carr, N. L.; Bell, A. T. Mass Transfer Coefficients and Solubilities for hydrogen and carbon monoxide under Fischer–Tropsch conditions. *Chem. Eng. Sci.* **1984**, *39*, 905.

Al-Dahhan, M. H.; Duduković, M. P. Pressure Drop and Liquid Hold-up in High Pressure Trickle-Bed Reactors. *Chem. Eng. Sci.* **1994**, *49*, 5681.

Al-Dahhan, M. H.; Duduković, M. P. Catalyst Wetting Efficiency in Trickle-Bed Reactors at High Pressure. *Chem. Eng. Sci.* **1995**, *50*, 2377.

Al-Dahhan, M. A.; Duduković, M. P. Catalyst Bed Dilution for Improving Catalyst Wetting in Laboratory Trickle-Bed Reactors. *AIChE J.* **1996**, *42*, 2594.

Bakos, M.; Arva, P.; Szeifert, F. Interfacial Area in Packed Bed Gas–Liquid Reactors with Cocurrent Downflow. *Hung. J. Ind. Chem.* **1980**, *8*, 383.

Barnes, H. A.; Hutton, J. F.; Walters, K. *An Introduction to Rheology*; Elsevier: Oxford, U.K., 1989.

Bentley, B. J.; Leal, L. G. An experimental investigation of drop deformation and break-up in steady, two-dimensional linear flows. *J. Fluid Mech.* **1986**, *167*, 241.

Bichari, M.; Roizard, C.; Midoux, N. Détermination des Coefficients de Transfert de Matière Côté Liquide et Côté Gaz dans une Cuve Agitée sous Pression. (Determination of Liquid-Side and Gas-Side Mass Transfer Coefficients in a High Pressure Stirred Vessel.) *Récents Prog. Génie Proc.* **1991**, *3*, 159.

Bichari, M.; Roizard, C.; Midoux, N. Détermination des Solubilités et des Coefficients de Transfert de Matière dans un Réacteur Agité sous Pression. (Gas Solubility and Mass Transfer Coefficients in a High Pressure Stirred Reactor.) *Récents Prog. Génie Proc.* **1993**, *7*, 79.

Bichari, M.; Roizard, C.; Laurent, A.; Midoux, N. Determination of the Volumetric Gas-Liquid Mass Transfer Coefficients at Pressure up to 5 MPa in Stirred Vessels. In *3rd International Symposium on High Pressure Chemical Engineering*, Zürich, Switzerland, Oct 7–9, 1996; Rudolf von Rohr, Ph., Trepp, Ch., Eds.; Elsevier B. V.: Amsterdam, The Netherlands, 1996; Vol. 12, p 169.

Blauwhoff, P. M.; van Swaaij, W. P. M. Gas–Liquid Equilibria-Between $H_2S$, $CO_2$ and Aqueous Amine Solutions. *2nd International Conference on Phase Equilibria and Fluid Properties in the Chemical Industry*; EFCE Publication 11: Berlin, 1980; Part I, p 78.

Blauwhoff, P. M.; Bos, M. Dissociation Constants of Diethanolamine and Diisopropanolamine in an Aqueous 1.00 M Potassium Chloride Solution. *J. Chem. Eng. Data* **1981**, *26*, 7.

Cassanello, M.; Larachi, F.; Laurent, A.; Wild, G.; Midoux, N. Gas–Liquid Mass Transfer in High Pressure Trickle-Bed Reactors: Experiments and Modeling. In *3rd International Symposium on High Pressure Chemical Engineering*, Zürich, Switzerland, Oct 7–9, 1996; Rudolf von Rohr, Ph., Trepp, Ch., Eds.; Elsevier B. V.: Amsterdam, The Netherlands, 1996; Vol. 12, p 493.

Chang, M.-Y.; Morsi, B. I. Mass transfer characteristics of gases in *n*-decane at elevated pressures and temperatures in agitated reactors. *Chem. Eng. J.* **1991a**, *47*, 33.

Chang, M.-Y.; Morsi, B. I. Mass transfer characteristics of gases in aqueous and organic liquids at elevated pressures and temperatures in agitated reactors. *Chem. Eng. Sci.* **1991b**, *46*, 2639.

Chang, M.-Y.; Morsi, B. I. Mass Transfer in a Three-Phase Reactor Operating at Elevated Pressures and Temperatures. *Chem. Eng. Sci.* **1992**, *47*, 1779.

Chang, M.-Y.; Eiras, J. G.; Morsi, B. I. Mass transfer characteristics in *n*-hexane at elevated pressures and temperatures in agitated reactors. *Chem. Eng. Proc.* **1991**, *29*, 49.

Charpentier, J. C. Recent Progress in Two-Phase Liquid Mass Transfer in Packed Beds. *Chem. Eng. J.* **1976**, *11*, 161.

Crine, M.; Marchot, P.; L'Homme, G. Statistical Hydrodynamics in Trickle Flow Columns. *AIChE J.* **1992**, *38*, 136.

Danckwerts, P. V. *Gas–liquid Reactions*; McGraw-Hill: New York, 1970.

Danckwerts, P. V.; Sharma, M. M. The absorption of carbon dioxide into solutions of alkalis and amines (with some notes on hydrogen sulphide and carbonyl sulphide). *Chem. Eng.* **1966**, *10*, 244.

Dankworth, D. C.; Kevrekidis, I. G.; Sundaresan, S. Dynamics of Pulsing Flow in Trickle Beds. *AIChE J.* **1990**, *36*, 605.

Deimling, A.; Karandikar, B. M.; Shah, Y. T.; Carr, N. L. Solubility and Mass transfer of CO and $H_2$ in Fischer-Tropsch liquids and slurries. *Chem. Eng. J.* **1984**, *29*, 127.

Edwards, T. J.; Maurer, G.; Newman, J.; Prausnitz, J. M. Vapor–liquid equilibria in multicomponent aqueous solutions of volatile weak electrolytes. *AIChE J.* **1978**, *24*, 966.

Fukushima, S.; Kusaka, K. Interfacial Area and Boundary of Hydrodynamic Flow Region in Packed Column with Cocurrent Downward Flow. *J. Chem. Eng. Jpn.* **1977**, *10*, 461.

Gianetto, A.; Specchia, V.; Baldi, G. Absorption in Packed Bed Towers with Concurrent Downward High-Velocity Flows—II: Mass Transfer. *AIChE J.* **1973**, *19*, 916.

Hinze, J. O. Fundamentals of the Hydrodynamic Mechanism of Splitting in Dispersion Processes. *AIChE J.* **1955**, *1*, 289.

Hirose, T.; Toda, M.; Sato, Y. Liquid Phase Mass Transfer in Packed Bed Reactor With Cocurrent Gas-Liquid Downflow. *J. Chem. Eng. Jpn.* **1974**, *7*, 187.

Holub, R. A.; Duduković, M. P.; Ramachandran, P. A. Pressure Drop, Liquid Holdup and Flow Regime Transition in Trickle Flow. *AIChE J.* **1993**, *39*, 302.

Karandikar, B. S.; Morsi, B. I.; Shah, Y. T.; Carr, N. L. Effect of water on the solubility and mass transfer coefficient of CO and $H_2$ in a Fischer–Tropsch liquid. *Chem. Eng. J.* **1986**, *33*, 157.

Koneripalli, N.; Tekie, Z.; Morsi, B. I.; Chang, M.-Y. Mass transfer characteristics of gases in methanol and ethanol under elevated pressures and temperatures. *Chem. Eng. J.* **1994**, *54*, 63.

Krichevsky, I. R.; Kasarnovsky, J. S. Thermodynamical Calculations of Solubilities of Nitrogen and Hydrogen in Water at High Pressures. *J. Am. Chem. Soc.* **1935**, *57*, 2168.

Larachi, F. *Les Réacteurs Triphasiques à Lit Fixe à Écoulement à Co-courant vers le Bas et vers le Haut de Gaz et de Liquide. Etude de l'Influence de la Pression sur l'Hydrodynamique et le Transfert de Matière Gaz-Liquide.* Ph.D. Thesis, INPL, Nancy, France, 1991.

Larachi, F.; Laurent, A.; Midoux, N.; Wild, G. Experimental study of a trickle-bed reactor operating at high pressure: Two-phase pressure drop and liquid saturation. *Chem. Eng. Sci.* **1991**, *46*, 1233.

Larachi, F.; Laurent, A.; Wild, G.; Midoux, N. Pressure effects on gas–liquid interfacial areas in cocurrent trickle-flow reactors. *Chem. Eng. Sci.* **1992**, *47*, 2325.

Larachi, F.; Wild, G.; Laurent, A.; Midoux, N. Influence of Gas Density on the Hydrodynamics of Cocurrent Gas–Liquid Upflow Fixed-Bed Reactors. *Ind. Eng. Chem. Res.* **1994**, *33*, 519.

Lara-Marquez, A.; Larachi, F.; Wild, G.; Laurent, A. Mass transfer characteristics of fixed beds with cocurrent upflow and downflow. A special reference to the effect of pressure. *Chem. Eng. Sci.* **1992**, *47*, 3485.

Ledakowitcz, S.; Nettelhof, H.; Deckwer, W.-D. Gas–liquid mass transfer data in a stirred autoclave reactor. *Ind. Eng. Chem. Fundam.* **1984**, *23*, 510.

Lee, J. H.; Foster, N. R. Mass transfer of Oxygen and Methane in Silicone Fluids and Perfluoroalkyl Polyether. *Ind. Eng. Chem. Res.* **1990a**, *29*, 1962.

Lee, J. H.; Foster, N. R. Mass transfer and Solubility of $O_2$ and $CH_4$ in Silicone Fluids. *Ind. Eng. Chem. Res.* **1990b**, *29*, 691.

Midoux, N.; Morsi, B. I.; Purwasasmita, M.; Laurent, A.; Charpentier, J. C. Interfacial Area and Liquid-Side Mass Transfer Coefficient in Trickle-Bed Reactors Operating with Organic Liquids. *Chem. Eng. Sci.* **1984**, *39*, 781.

Miller, S. A.; Ekstrom, A.; Foster, N. R. Solubility and Mass Transfer Coefficients for Hydrogen and Carbon Monoxide in *n*-Octacosane. *J. Chem. Eng. Data* **1990**, *35*, 125.

Mizan, T. I.; Li, J.; Morsi, B. I.; Chang, M.-Y.; Maier, E.; Singh, C. P. P. Solubilities and Mass Transfer Coefficients of Gases in Liquid Propylene in a Surface-Aeration Agitated Reactor. *Chem. Eng. Sci.* **1994**, *49*, 821.

Molga, E. J.; Westerterp, K. R. Gas–Liquid Interfacial Area and Holdup in a Cocurrent Upflow Packed-Bed Bubble-Column Reactor at Elevated Pressures. *Ind. Eng. Chem. Res.* **1997**, *36*, 622.

Morsi, B. I. Mass Transfer Coefficients in Trickle-Bed Reactor with High and Low Viscosity Organic Solutions. *Chem. Eng. J.* **1989**, *41*, 41.

Morsi, B. I.; Laurent, A.; Midoux, N.; Charpentier, J. C. Interfacial Area in Trickle-Bed Reactors: Comparison Between Ionic and Organic Liquids and Between Raschig Rings and Small Diameter Particles. *Chem. Eng. Sci.* **1980**, *35*, 1467.

Morsi, B. I.; Laurent, A.; Midoux, N.; Barthole-Delauney, G.; Storck, A.; Charpentier, J.-C. Hydrodynamics and gas–liquid–solid parameters of cocurrent Downward two-phase flow in trickle-bed reactors. *Chem. Eng. Commun.* **1984**, *25*, 267.

Ng, K. M. A Model for Flow Regime Transitions in Cocurrent Downflow Trickle-Bed Reactors. *AIChE J.* **1986**, *32*, 115.

Oyevaar, M. H.; Morssinkhoff, R. W. J.; Westerterp, K. R. Density, viscosity, solubility and diffusivity of $CO_2$ and $N_2O$ in solutions of diethanolamine in aqueous ethylene-glycol at 298 K. *J. Chem. Eng. Data* **1989**, *34*, 77.

Oyevaar, M. H.; Morssinkhoff, R. W. J.; Westerterp, K. R. The kinetics of the reaction between $CO_2$ and diethanolamine in aqueous ethylene-glycol at 298 K: A viscous gas–liquid reaction system for the determination of interfacial areas in gas–liquids contactors. *Chem. Eng. Sci.* **1990**, *45*, 3283.

Oyevaar, M. H.; Bos, R.; Westerterp, K. R. Interfacial areas and gas holdups in gas–liquid contactors at elevated pressures from 0.1 to 8.0 MPa. *Chem. Eng. Sci.* **1991**, *46*, 1217.

Pinsent, B. R. W.; Pearson, L.; Roughton, F. J. W. The kinetics of combination of carbon dioxide with hydroxide ions. *Trans. Faraday Soc.* **1956**, *52*, 1512.

Reid, R. C.; Prausnitz, J. M.; Poling, B. E. *The Properties of Gases and Liquids*; McGraw-Hill Book Co.: New York, 1987.

Stegeman, D.; Ket, P. J.; van der Kolk, H. A.; Bolk, J. W.; Knop, P. A.; Westerterp, K. R. Interfacial Area and Gas Hold-up in an Agitated Gas–Liquid Reactor under Pressure. *Ind. Eng. Chem. Res.* **1995**, *34*, 59.

Stegeman, D.; Knop, P. A.; Wijnands, A. J. G.; Westerterp, K. R. Interfacial Area and Gas Hold-up in an Bubble Column Reactor at Elevated Pressure. *Ind. Eng. Chem. Res.* **1996**, *35*, 3842.

Stüber, F.; Wilhelm, A. M.; Delmas, H. Modelling of Three-Phase Catalytic Upflow Reactor: A Significant Chemical Determination of Liquid–Solid and Gas–Liquid Mass Transfer Coefficients. *Chem. Eng. Sci.* **1996**, *51*, 2161.

Taylor, G. I. The Formation of Emulsions in Definable Fields of Flow. *Proc. R. Soc. London, Ser. A* **1934**, *146*, 501.

Tekie, Z.; Li, J.; Morsi, B. I.; Chang, M. Y. Gas-Liquid Mass Transfer in Cyclohexane Oxidation Process Using Gas-Inducing and Surface-Aeration Agitated Reactors. *Chem. Eng. Sci.* **1997**, *52*, 1541.

Teramoto, M.; Tai, S.; Nishii, K.; Teranishi, H. Effects of pressure on liquid-phase mass transfer coefficients. *Chem. Eng. J.* **1974**, *8*, 223.

Toppinen, S.; Aittamaa, J.; Salmi, T. Interfacial Mass Transfer in Trickle-Bed Reactor Modelling. *Chem. Eng. Sci.* **1996**, *51*, 4335.

Torza, S.; Cox, R. G.; Mason, S. G. Particle motions in sheared suspensions: XXVII. Transient and steady deformation and burst of liquid drops. *J. Colloid Interface Sci.* **1972**, *38*, 395.

Tseng, T. T.; Ho, W. S.; Savage, D. W. Carbon dioxide absorption into promoted carbonate solutions. *AIChE J.* **1988**, *34*, 922.

Utracki, L. A.; Shi, Z. H. Development of polymer blend morphology during compounding in a twin-screw extruder. Part I: Droplet dispersion and coalescence—a review. *Polym. Eng. Sci.* **1992**, *32*, 1824.

Vafopoulos, I.; Szatecsny, K.; Moser, F. Der Einfluss des Partial und Gesamtdruckes auf den Stoffaustausch. *Chem. Ing. Tech.* **1975**, MS 266.

Venkata Ratnam, G. S.; Varma, Y. B. G. Effective Interfacial Area in Gas–Liquid Cocurrent Downflow Through Packed Beds. *Bioproc. Eng.* **1991**, *7*, 29.

Venkata Ratnam, G. S.; Venkata Narasaiah, D.; Varma, Y. B. G. A Correlation for Interfacial Area in Cocurrent Gas-Liquid Downflow Through Packed Beds. *Bioproc. Eng.* **1994**, *10*, 53.

Versteeg, G. F. Mass Transfer and Chemical Reaction Kinetics in Acid Gas Treating Processes. Ph.D. Thesis, Twente University, Enschede, The Netherlands, 1987.

Versteeg, G. F.; van Swaaij, W. P. M. On the kinetics between $CO_2$ and alkanolamines both in aqueous and non-aqueous solutions. I: Primary and secondary amines. *Chem. Eng. Sci.* **1988**, *43*, 573.

Versteeg, G. F.; Blauwhoff, P. M. M.; van Swaaij, W. P. M. The effect of diffusivity on gas–liquid mass transfer in stirred vessels. Experiments at atmospheric and elevated pressures. *Chem. Eng. Sci.* **1987**, *42*, 1103.

Versteeg, G. F.; Kuipers, J. A. M.; van Beckum, F. P. H; van Swaaij, W. P. M. Mass Transfer with Complex Reversible Chemical Reaction. Single Reversible Reactions. *Chem. Eng. Sci.* **1989**, *44*, 2295.

Wammes, W. J. A.; Westerterp, K. R. Hydrodynamics in a Pressurized Cocurrent Gas–Liquid Trickle-Bed Reactor. *Chem. Eng. Technol.* **1991**, *14*, 406.

Wammes, W. J. A.; Middelkamp, J.; Huisman, W. J.; deBaas, C. M.; Westerterp, K. R. Hydrodynamics in a Cocurrent Gas–Liquid Trickle Bed at Elevated Pressures. *AIChE J.* **1991**, *37*, 1849.

Wild, G.; Larachi, F.; Charpentier, J.-C. Heat and Mass Transfer in Gas–Liquid–Solid Fixed Bed Reactors. In *Heat and Mass Transfer in Porous Media*; Quintard, M., Todorović, M., Eds.; Elsevier: Amsterdam, The Netherlands, 1992; p 616.

Wilkinson, P. M.; Haringa, H.; van Dierendonck, L. L. Mass Transfer and Bubble Size in a Bubble Column under Pressure. *Chem. Eng. Sci.* **1994**, *49*, 1417.

Yaïci, W.; Laurent, A.; Midoux, N.; Charpentier, J. C. Determination of gas-side mass transfer coefficients in trickle-bed reactors in the presence of an aqueous or an organic liquid phase. *Int. Chem. Eng.* **1988**, *28*, 299.

Yoshida, F.; Arakawa, S. Pressure dependence of liquid-phase mass transfer coefficients. *AIChE J.* **1968**, *14*, 962.

Zemaitis, J. F.; Clark, D. M.; Rafal, M.; Scrivner, N. C. *Handbook of Aqueous Electrolyte Thermodynamics. Theory and Applications*; DIPPR, AIChE: New York, 1986.

*Received for review* December 23, 1996
*Revised manuscript received* May 31, 1997
*Accepted* June 17, 1997

IE960903U